Published in final edited form as:

Immunity. 2020 May 19; 52(5): 825–841.e8. doi:10.1016/j.immuni.2020.04.014.

Developmental Relationships of Four Exhausted CD8+ T Cell Subsets Reveals Underlying Transcriptional and Epigenetic Landscape Control Mechanisms

Jean-Christophe Beltra[1,2,3], **Sasikanth Manne**[1,2], **Mohamed S. Abdel-Hakeem**[1,2,3,4], **Makoto Kurachi**[5], **Josephine R. Giles**[1,2,3], **Zeyu Chen**[1,2], **Valentina Casella**[6], **Shin Foong Ngiow**[1,2,3], **Omar Khan**[1,2,7], **Yinghui Jane Huang**[1,2], **Patrick Yan**[1,2,7], **Kito Nzingha**[1,2], **Wei Xu**[8,9], **Ravi K. Amaravadi**[8,9], **Xiaowei Xu**[9,10], **Giorgos C. Karakousis**[9,11], **Tara C. Mitchell**[8,9], **Lynn M. Schuchter**[8,9], **Alexander C. Huang**[2,3,8,9], **E. John Wherry**[1,2,3,12,*]

[1]Department of Systems Pharmacology and Translational Therapeutics, Perelman School of Medicine, University of Pennsylvania, Philadelphia, PA, USA

[2]Institute for Immunology, Perelman School of Medicine, University of Pennsylvania, Philadelphia, PA, USA

[3]Parker Institute for Cancer Immunotherapy at University of Pennsylvania, Philadelphia, PA, USA

[4]Department of Microbiology and Immunology, Faculty of Pharmacy, Cairo University, Kasr El-Aini, Cairo, Egypt

[5]Department of Molecular Genetics, Graduate School of Medical Sciences, Kanazawa University, Kanazawa, Japan

[6]Infection Biology Laboratory, Department of Experimental and Health Sciences (DCEXS), Universitat Pompeu Fabra, Barcelona, Spain

[7]Arsenal Biosciences, South San Francisco, CA, USA

[8]Department of Medicine, Perelman School of Medicine, University of Pennsylvania, Philadelphia, PA, USA

[9]Abramson Cancer Center, Perelman School of Medicine, University of Pennsylvania, Philadelphia, PA, USA

[10]Department of Pathology and Laboratory Medicine, Perelman School of Medicine, University of Pennsylvania, Philadelphia, PA, USA

[*]Correspondence: wherry@pennmedicine.upenn.edu.

AUTHOR CONTRIBUTIONS

J.-C.B. and E.J.W. designed the experiments. J.-C.B. performed and analyzed the experiments with help from M.A.-H., V.C., and K.N. J.G. processed the ATAC-seq data. S.M. and J.-C.B. analyzed RNA-seq and ATAC-seq data. M.K., J.-C.B., S.F.N., and O.K. produced RV. Z.C. and Y.J.H. developed *Tcf7cKO* and $Tox^{+/-}$ mice. P.Y. and A.C.H. analyzed human samples. W.X., R.K.A., X.X., G.C.K., T.C.M., and L.M.S. coordinated human sample collection. J.-C.B. and E.J.W. wrote the manuscript.

DECLARATION OF INTERESTS

E.J.W. is a member of the Parker Institute for Cancer Immunotherapy which supported these studies. E.J.W. has consulting agreements with and/or is on the scientific advisory board for Merck, Roche, Pieris, Elstar, and Surface Oncology. E.J.W. has a patent licensing agreement on the PD-1 pathway with Roche/Genentech. E.J.W. is a founder of Arsenal Biosciences.

SUPPLEMENTAL INFORMATION

Supplemental Information can be found online at https://doi.org/10.1016/j.immuni.2020.04.014.

[11]Department of Surgery, Perelman School of Medicine, University of Pennsylvania, Philadelphia, PA, USA

[12]Lead Contact

SUMMARY

$CD8^+$ T cell exhaustion is a major barrier to current anti-cancer immunotherapies. Despite this, the developmental biology of exhausted $CD8^+$ T cells (Tex) remains poorly defined, restraining improvement of strategies aimed at "re-invigorating" Tex cells. Here, we defined a four-cell-stage developmental framework for Tex cells. Two $TCF1^+$ progenitor subsets were identified, one tissue restricted and quiescent and one more blood accessible, that gradually lost TCF1 as it divided and converted to a third intermediate Tex subset. This intermediate subset re-engaged some effector biology and increased upon PD-L1 blockade but ultimately converted into a fourth, terminally exhausted subset. By using transcriptional and epigenetic analyses, we identified the control mechanisms underlying subset transitions and defined a key interplay between TCF1, T-bet, and Tox in the process. These data reveal a four-stage developmental hierarchy for Tex cells and define the molecular, transcriptional, and epigenetic mechanisms that could provide opportunities to improve cancer immunotherapy.

Graphical Abstract

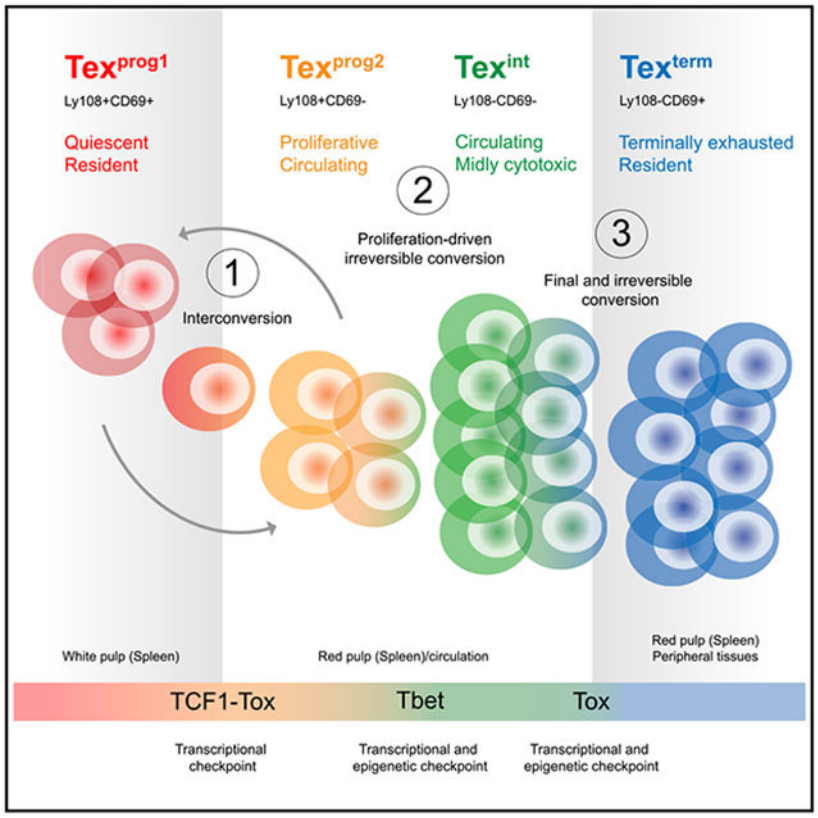

In Brief

Beltra et al. define a hierarchical developmental pathway for $CD8^+$ T cell exhaustion, revealing four stages and multistep transcriptional and epigenetic dynamics underlying subset transitions and subset-associated biological changes.

INTRODUCTION

Chronic viral infections (HIV, HCV, HBV) and cancers subvert $CD8^+$ T cell differentiation toward exhaustion. $CD8^+$ T cell exhaustion has a central role in these settings because blockade of the PD-1 inhibitory receptor (IR) pathway reinvigorates exhausted $CD8^+$ T cells (Tex) and improves immune control of chronic infections and cancer (McLane et al., 2019). Conversely, as exhaustion gets more severe, clinical symptoms of autoimmunity decrease (McKinney et al., 2015). Indeed, Tex cells are a major cell type responding to PD-1 blockade (Huang et al., 2017; Miller et al., 2019; Siddiqui et al., 2019; Thommen et al., 2018), and trials are underway to reinvigorate Tex cells in human chronic viral infections (Wykes and Lewin, 2018). A hallmark of Tex populations is heterogeneity (Blackburn et al., 2008; He et al., 2016; Im et al., 2016; Paley et al., 2012; Utzschneider et al., 2016; Wu et al., 2016). This heterogeneity is relevant for disease because the distribution of these Tex subsets in tumors could relate to response to checkpoint blockade (Daud et al., 2016; Huang et al., 2019; Huang et al., 2017; Kurtulus et al., 2019; Sade-Feldman et al., 2019). Despite the clinical importance of Tex cells, our understanding of their developmental biology and underlying cellular and molecular mechanisms regulating their formation, maintenance, and response to immunotherapies remains incomplete.

PD-1-intermediate Tex progenitors selectively respond to PD-1 pathway blockade, whereas PD-1-high Tex cells are terminally exhausted and do not respond (Blackburn et al., 2008). A developmental hierarchy was defined in which the progenitor Tex subset self-renews and also gives rise to the more terminal Tex subset through proliferation (Paley et al., 2012). T cell factor family member TCF1 (*Tcf7*) is a key transcription factor (TF) for the progenitor Tex population (Chen et al., 2019; Im et al., 2016; Utzschneider et al., 2016; Wu et al., 2016). However, different studies used distinct markers to define Tex subsets (e.g., PD-1, the T-box TFs T-bet and Eomes, or CXCR5 and Tim-3), but inconsistencies between the proposed models suggest a more heterogeneous Tex subset landscape and developmental biology (Im et al., 2016; Paley et al., 2012; Utzschneider et al., 2016). Indeed, recent studies of $CX3CR1^+$ Tex populations (Hudson et al., 2019; Zander et al., 2019) and high-dimensional single-cell profiling of Tex cells in humans and mice (Kurtulus et al., 2019; Li et al., 2019; Miller et al., 2019; Sade-Feldman et al., 2019; Zander et al., 2019) indicate a more complex Tex subset biology.

The transcriptional and epigenetic landscape of Tex cells defines exhaustion as a distinct branch of $CD8^+$ T cell differentiation (Pauken et al., 2016; Philip et al., 2017; Scott-Browne et al., 2016; Sen et al., 2016). The high-mobility group (HMG)-protein Tox drives epigenetic programming of Tex cells and establishes the exhaustion-specific epigenetic landscape (Alfei et al., 2019; Khan et al., 2019; Scott et al., 2019; Seo et al., 2019; Yao et al., 2019). Tex cells maintain high Tox at late time points of chronic viral infections and cancer. Nevertheless, the role of Tox has only been defined during initiation of

Tex cell development, and the impact of this TF once Tex cells have been established remains unclear. Moreover, one consequence of a stable epigenetic identity of Tex cells is that interventions such as PD-1 pathway blockade only provide temporary benefit by reactivating existing transcriptional circuits (Pauken et al., 2016). These reinvigorated Tex cells, however, are not epigenetically reprogrammed and reacquire their exhausted features over time (Pauken et al., 2016). A major question is whether Tex cell heterogeneity can be exploited to achieve better efficacy of immunotherapies. However, the key steps in Tex cell differentiation, underlying TFs, and epigenetic landscape changes involved remain to be defined.

To address these questions, we used chronic lymphocytic choriomeningitis virus (LCMV) infection in mice and performed complementary analysis in mouse and human tumors. We defined four distinct Tex subsets based on Ly108 (*Slamf6*) and CD69 expression and linked these subsets in a hierarchical developmental scheme. Two interconverting $TCF1^+$ progenitor cell-states were identified: one quiescent and blood inaccessible and a second that initiated robust cell cycling and gained access to circulation. This second $TCF1^+$ Tex subset gave rise to a $TCF1^-$ T-bet^{hi} intermediate Tex subset that (re)acquired some effector-like features. These intermediate Tex cells ultimately became terminally differentiated, losing T-bet (and gaining Eomes) and permanently exiting cell cycle. This final transition was coordinated by Tox-mediated antagonism of T-bet. PD-1 pathway blockade preferentially expanded the second progenitor and the T-bet^{hi} intermediate Tex subsets. These data help clarify previous Tex subset models by defining additional heterogeneity and connecting this heterogeneity to differentiation and underlying transcriptional and epigenetic control.

RESULTS

Ly108 (*Slamf6*) and CD69 Define Four Tex Subsets during Chronic Viral Infection and Cancer

To interrogate Tex cell heterogeneity, we first analyzed adoptively transferred LCMV $D^bGP_{33\text{-}41}$-specific P14 $CD8^+$ T cells in LCMV-clone-13-infected mice. At day 30 post-infection (d30pi), P14 cells could be separated into PD-1 intermediate (PD-1^{int}) and PD-1 high (PD-1^{hi}) subsets (Figure 1A) (Blackburn et al., 2008). PD-1^{int} Tex cells could be further subdivided by TCF1 expression (Figure 1A) identifying PD-$1^{int}TCF1^+$, PD-1^{int} $TCF1^-$, and PD-$1^{hi}TCF1^-$ cells. PD-$1^{int}TCF1^-$ cells were more abundant than either PD-1^{hi} or PD-$1^{int}TCF1^+$ populations and displayed evidence of recent proliferation *in vivo*, reminiscent of an active developmental transition (Figures S1A and S1B) (Paley et al., 2012). Proliferating cells were also observed in the PD-$1^{int}TCF1^+$ population, whereas few PD-1^{hi} cells were $Ki67^+$ (Figures 1B and S1B). CD69 distinguished PD-1^{int} $TCF1^-$ cells ($CD69^-$) from the PD-1^{hi} Tex subset ($CD69^+$), and expression of CD69 was anti-correlated with proliferation (Figures 1B and S1C). CD69 expression also correlated with Tox and Eomes but was negatively associated with T-bet (Figures 1C and S1D). CD69 also demarcated a fraction of $TCF1^+$ cells that preferentially lacked Ki67 expression (Figures 1B, 1C, and S1E). Thus, combining CD69 with Ly108 (*Slamf6*), a surrogate of TCF1 expression (Figure S1F) identified four Tex subpopulations: $Ly108^+CD69^+$, $Ly108^+CD69^-$, $Ly108^-CD69^-$ and $Ly108^-CD69^+$ in chronic, but not acute, infection

(Figure 1D). This pattern was present at all time points, was also observed for non-T cell receptor (TCR) transgenic responses, and was seen in multiple organs, although different subsets were enriched in different tissues (Figures 1D-1G and S1G). TCF1 expression was lost as Ki67 increased, peaking in the Ly108^{-}CD69^{-} population before declining in the Ly108^{-}CD69^{+} subset. This latter subset was consistent with PD-1^{hi} terminal Tex cells (Figure 1H). The Ly108^{+}CD69^{+} subset had higher TCF1 but low *ex vivo* Ki67 in comparison with Ly108^{+}CD69^{-} cells (Figure 1H). Hence, differential CD69 expression distinguished quiescent (Ly108^{+}CD69^{+}) and cycling (Ly108^{+}CD69^{-}) TCF1^{+} Tex subsets. A similar pattern of four Tex subsets was found in mouse B16 tumors and also for tumor-infiltrating lymphocytes (TILs) from human melanoma (Figures 1I,1J, and S1H-S1K). Thus, we identified four Tex subsets based on Ly108 (or TCF1) and CD69 expression in mice and humans.

Developmental Relationships between the Four Ly108- and CD69-Defined Tex Subsets

To next investigate lineage relationships, we adoptively transferred sorted and CFSE-labeled Tex subsets into infection-matched recipients (Figures 2A and S2A). After seven days, the Ly108^{+}CD69^{+} donor population gave rise to the most divided cells followed by the Ly108^{+}CD69^{-} subset. Both populations persisted better *in vivo* than did the Ly108^{-} subsets and regenerated all four Tex populations (Figures 2B, 2C, S2B, and S2C). Notably, the Ly108^{+}CD69^{-} Tex subset also gave rise to Ly108^{+}CD69^{+} cells (Figure 2C). Ly108^{-}CD69^{-} and Ly108^{-}CD69^{+} transferred cells divided poorly, had limited persistence, and restrained developmental plasticity (Figures 2B, 2C, S2B, and S2C). The Ly108^{-}CD69^{-} cells also mainly retained their identity and gave rise to Ly108^{-}CD69^{+} cells. Donor Ly108^{-}CD69^{+} cells gave rise to essentially no proliferated progeny and mainly retained their original state (Figures 2B and 2C). The few Ly108^{-}CD69^{-} cells recovered from the Ly108^{-}CD69^{+} donor population likely reflected few contaminating Ly108^{-}CD69^{-} cells in the donor pool (though some inter-conversion cannot be excluded). Neither of the Ly108^{-} subsets gave rise to Ly108^{+} cells, consistent with irreversible commitment when TCF1 was lost. Based on the undivided (CFSE^{hi}) transferred cells, Ly108^{+}CD69^{+} and Ly108^{+}CD69^{-} donor Tex cells were capable of generating each other (Figures 2D, S2D, and S2E). Ly108^{+}CD69^{-} cells accumulated more than the Ly108^{+}CD69^{+} in the divided (CFSE^{lo}) fraction independently of the donor population (Figures 2D, 2E, S2D, and S2E). Accordingly, Ly108^{+}CD69^{+} donor cells that retained their identity after seven days had undergone few cell divisions, whereas the Ly108^{+}CD69^{-} progeny from these donor cells had proliferated extensively (Figure S2F). Hence, Ly108^{+}CD69^{+} cells had features of quiescent progenitors and restrained *in vivo* cell cycle (Figure 1H). Thus, Ly108^{+}CD69^{+} cells likely first passively transitioned to a secondary Ly108^{+}CD69^{-} stage. Extensive proliferation then occurred with the formation of Ly108^{-}CD69^{-} cells (Figures 1H and 2D). Although a low frequency of Ly108^{-}CD69^{-} cells could be detected without proliferation from Ly108^{+}CD69^{+} (13.9%) or Ly108^{+}CD69^{-} (16.2%) donor cells, the proportion of the Ly108^{-}CD69^{-} subset increased substantially with proliferation, outnumbering Ly108^{+}CD69^{-} cells among the dividing cells (Figures 2D, S2D, S2E, and S2G). The high Ki67 expression found at steady state in Ly108^{-}CD69^{-} cells (Figure 1H) contrasted their lack of proliferative potential in this setting (Figure 2B), suggesting that this population arises from dividing Ly108^{+}CD69^{-} progenitors and loses further proliferative potential. Lastly, the few cells recovered from the donor Ly108^{-}CD69^{+}

cells remained undivided and largely conserved their original identity (Figures 2B-2D and S2B-S2E). Ly108^{-}CD69^{+} cells could also be generated from all other subsets (Figures 2C, 2D, S2D, and S2E). The minor Ki67 expression found in the Ly108^{-}CD69^{+} subset coupled with the lack of proliferative potential of Ly108^{-}CD69^{-} cells suggested that the former cells differentiate from the post-mitotic fraction of Ly108^{-}CD69^{-} cells. Co-expression of IRs and phenotypic changes consistent with terminal exhaustion accompanied the progression from Ly108^{+}CD69^{+} → Ly108^{+}CD69^{-} → Ly108^{-}CD69^{-} → Ly108^{-}CD69^{+} (Figures 2F and 2G). For clarity, these Tex subsets will be referred to here as progenitor 1 (Ly108^{+}CD69^{+}; Tex^{prog1}), progenitor 2 (Ly108^{+}CD69^{-}; Tex^{prog2}), intermediate (Ly108^{-}CD69^{-}; Tex^{int}), and terminal (Ly108^{-}CD69^{+}; Tex^{term}).

PD-L1 Blockade Selectively Expands Transitioning Tex Subsets

PD-1/PD-L1 pathway blockade likely impacts Tex subset distribution. Thus, we interrogated changes in the four Tex subsets after PD-L1 blockade (Figure S2H). In the absence of CD4^{+} T cell help, the Tex^{prog2} and Tex^{int} subsets were reduced in comparison with the CD4-sufficient settings at d30pi (Figures S2I and S2J) (Zander et al., 2019). PD-L1 blockade preferentially promoted accumulation of the Tex^{prog2} and Tex^{int} subsets. One day after treatment, the absolute number of Tex^{prog1} and Tex^{term} cells increased 2.1- and 2.2-fold, respectively, whereas the number of Tex^{prog2} and Tex^{int} cells increased 17- and 10-fold, respectively (Figures 2H and 2I). These data indicate that Tex cell reinvigoration by PD-1 pathway blockade partially rebalanced Tex subset distribution by fostering the formation of the Tex^{prog2} and Tex^{int} subsets.

Dynamic Changes in T-bet and Eomes in Four Subsets of Tex Cells

We previously identified differences in T-bet and Eomes expression in Tex subsets (Figure S3A) (Paley et al., 2012). More recent studies that defined Tex subsets based on CXCR5 and Tim-3 found a different expression pattern for T-bet and Eomes (Figure S3A) (Im et al., 2016; Utzschneider et al., 2016). We therefore asked whether the four-stage developmental hierarchy defined above could better resolve the dynamics of T-bet and Eomes in Tex cells. First, gating on Tex subsets based on PD-1 versus CXCR5 and Tim-3 revealed different patterns of the four subsets defined by Ly108 and CD69. CXCR5^{+} Tex captured Tex^{prog1} and Tex^{prog2} cells whereas the PD-1^{int} population also contained the Tex^{int} subset (Figure S3B). This Ly108^{-}CD69^{-} Tex^{int} subset was nearly completely absent from the PD-1^{hi} population but was contained in the subset defined as CXCR5^{-} (Figure S3B). Eomes was highest in Tex^{prog1} cells, declining slightly in Tex^{prog2} and even more in the Tex^{int} subset (Figures S3C-S3E). However, Eomes expression rebounded at the Tex^{term} stage (Figures S3C-S3H). T-bet expression, in contrast, gradually increased from Tex^{prog1} and was highest in Tex^{int} cells from both LCMV-infected mice and human tumors before dropping at the Tex^{term} stage (Figures S3C-S3H). Consistent with T-bet-repressing PD-1 (Kao et al., 2011), we observed a slight decrease in PD-1 at the Tex^{prog2} and Tex^{int} stages, whereas other IRs gradually increased from Tex^{prog1} to Tex^{term} (Figures 2F and S3I). Thus, the initial stages of Tex subset differentiation (i.e., from Tex^{prog1} to Tex^{int}) were accompanied by an Eomes^{hi} to T-bet^{hi} conversion concomitant with loss of TCF1 and decreased PD-1 expression, whereas the later transition to the Tex^{term} subset was accompanied by a T-bet^{hi} to Eomes^{hi} conversion and higher PD-1 expression.

Location and Function of Ly108- and CD69-Defined Tex Subsets

CXCR5-defined Tex progenitors (CXCR5$^+$) are resident of lymphoid tissues whereas CXCR5$^-$ Tex cells are found in circulation and peripheral organs (He et al., 2016; Im et al., 2016). Because the Tex subsets described above were defined by CD69 that can regulate lymphocyte egress, we next performed intravascular antibody (i.v. Ab) staining to assess blood accessibility (Anderson et al., 2014). Consistent with previous work (Beura et al., 2015), 73% (±2% SEM) of splenic P14 CD8$^+$ T cells were labeled by i.v. anti-CD8 Ab (Figures S4A and S4B). Tex^{prog1} cells, however, were almost exclusively (~80%) in the i.v. Ab$^-$ fraction, consistent with localization to the white pulp of the spleen (Figure 3A). In contrast, 47% (±2% SEM) of the Tex^{prog2} population was marked by i.v. Ab staining, indicating blood accessibility likely in the red pulp (Figure 3A). Moreover, a majority of Tex^{int} and Tex^{term} were i.v. Ab labeled (Figure 3A). The two CD69$^-$ subsets, Tex^{prog2} and Tex^{int}, were present in blood, whereas Tex^{prog1} and Tex^{term} cells were not (Figure 3B). Circulating Tex^{prog2} cells retained expression of TCF1 in the blood (Figure 3C). The absence of Tex^{term} cells in blood despite robust i.v. Ab staining suggested that these cells were resident of the blood-accessible splenic red pulp. Thus, the Ly108$^+$ (TCF-1$^+$) Tex^{prog1} and Tex^{prog2} subsets differed in anatomical location, with the latter gaining access to blood. The Tex^{int} subset was also highly blood accessible whereas the re-acquisition of CD69 expression by Tex^{term} cells was associated with tissue-residency but in distinct environments in comparison with Tex^{prog1} cells.

We next evaluated effector functions. Among the Tex subsets, Tex^{prog1} contained the highest frequency of IFNγ-producers, IFNγ and TNF coproducers (Figures 3D-3F) and also made the most IFNγ per cell (Figure S4C). Cytokine coproduction declined in Tex^{prog2} and Tex^{int} subsets (Figures 3D-3F and S4C) but then rebounded slightly at the Tex^{term} stage, although these cells were inferior to Tex^{prog1} on a per-cell basis (Figures 3D-3F and S4C). However, Tex^{int} and Tex^{term} accounted for a respective 49% and 34% of the absolute number of IFNγ-producing P14 cells, and Tex^{term} contributed the largest number of IFNγ and TNF co-producers (Figures S4D and S4E). Note, expression of Ly108 and CD69 on Tex cells was unaffected by peptide re-stimulation (Figures S4F and S4G), and memory T cells (Tmem) outperformed all Tex subsets (Figures 3D-3F and S4C). CD107a staining followed a similar trend to cytokine secretion profiles (Figures 3G and 3H). However, Tex^{int} and Tex^{term} cells mediated the most target killing (Figure S4H). *Ex vivo* proliferative potential was restricted to Tex^{prog1} and to a lesser extent Tex^{prog2} cells, although this proliferation was substantially worse than Tmem cells (Figure 3I). The robust proliferation of Tex^{prog1} cells upon antigen stimulation but evidence of low *in vivo* proliferation and relative lack of Ki67 (Figure 1H) pointed to a high proliferative potential but low ongoing cell cycle by this quiescent subset in the steady state. In contrast, Tex^{int} and Tex^{term} cells were almost incapable of undergoing cell division upon re-stimulation *in vitro* despite, at least for Tex^{int} cells, *ex vivo* Ki67 expression as evidence of recent *in vivo* cell cycling (Figure 3I). Tex^{prog1} and Tex^{prog2} cells also had little evidence of *ex vivo* cell death, whereas apoptotic cells were readily detectable for Tex^{int} and Tex^{term} subsets in both the LCMV system and human melanoma tumors (Figures 3J and S4I). Collectively, these data identify a specific set of functional properties for each Tex subset.

Transcriptional Programs of Tex Subsets

We next performed RNA sequencing (RNA-seq) to further define the biology of Tex subsets. Principal-component analysis (PCA) highlighted a distinct transcriptional program for each Tex subset defined by Ly108 and CD69, and each population also differed from conventional effector (Teff) or Tmem cells (Figures 4A and S5A). Pairwise comparisons defined differentially expressed genes (DEGs) and subset-specific transcriptional signatures (Figures 4B and S5B; Table S1). Tex subsets shared upregulated genes ($DEGs^{UP}$) with their direct neighbors from the developmental relationships above, but fewer with more distant subsets. For example, ~40% of Tex^{prog1} $DEGs^{up}$ were also up in Tex^{prog2} whereas few of these genes were shared by Tex^{int} and Tex^{term} cells (Figure 4C). We then asked how the Tex subset transcriptional signatures compared with previous Tex cell scRNA-seq data (Figure S5C) (Miller et al., 2019). Bi-clustering analysis classified DEGs from Ly108- and CD69-defined subsets into seven modules (Figure S5D, top row; Table S2). These DEGs modules were then mapped onto the scRNA-seq data (Figure S5D, bottom row). This analysis revealed similarity of Tex^{prog1} and Tex^{prog2} cells with a *Tcf7*$^{+}$ progenitor-like single cell cluster (Figures S5C and S5D; module 1), with broader mapping of the Tex^{prog2} signature in scRNA-seq space (Figures S5C and S5D; modules 3 and 4). DEGs from the Tex^{int} subset mapped mainly to a scRNA-seq cluster enriched for effector-like biology exemplified by genes like *Cx3cr1* (Figures S5C and S5D; module 5). DEGs biased to the Tex^{term} subset mapped mainly to the cluster identified as terminal Tex cells (Figures S5C and S5D; module 7). Thus, each Tex population had a distinct transcriptional program, and the relationship between these transcriptional signatures was consistent with the developmental scheme above.

To identify subset-specific biology, we clustered DEGs and examined gene ontology. Genes upregulated in Tex^{prog1} cells were involved in progenitor biology (*Tcf7*, *Myb*, *Il7r*, *Self*), Tfh biology (*Cxcr5*, *Icos*), and positive co-stimulation (*Cd28*) (Figure 4D, clusters 5 and 6; Table S3). Many of these genes were also expressed in Tex^{prog2}, but often at lower amounts (e.g., *Tcf7*, *Cxcr5*, *CD28*), an observation confirmed for protein (Figures 4D, 4F, S5E, and S5F). Cluster 5, biased to the Tex^{prog1} subset, also contained interferon-stimulated genes (ISGs) including *Irf7*, *Oas1*, and *Stat1* contributing to an enrichment for antiviral defense signatures (Figures 4D and 4E). Cluster 1 contained genes preferentially upregulated in Tex^{prog2} and was enriched for genes related to cell-cycle (e.g., cyclins and *mki67*) and cell motility (*Anxa2*, *Itgb7*, *Alcam*) (Figures 4D, 4E, and S5E). The transcriptional signature of Tex^{int} cells was enriched in clusters 3, 4, and 8, which contained effector-related genes (e.g., *Grzma*, *Grzmb*, *Prf1* [cluster 4]; *Klrg1* [cluster 3]; *Cx3cr1* [cluster 8]) and TFs (*Tbx21*, *Zeb2*, *Id2*, *Prdm1* [cluster 4]), with corresponding protein expression and gene ontology pathways (cluster 4) (Figures 4D-4F, S5E, and S5F). Cluster 3 also captured biology related to natural killer (NK) cells for Tex^{int} (e.g., *Klr* family genes). Lastly, Tex^{term} cells upregulated mRNA and protein for IRs (*Pdcd1*, *Lag3*, *Tigit*, *Cd244* [clusters 2 and 7]) and molecules associated with terminal exhaustion (*Entpd1*, *Cd101*, *Cd38* [clusters 2 and 7]). Cluster 2 was highly biased to Tex^{term} and enriched for pathways including negative regulation of cell activation (Figure 4E). Tex^{term} cells also showed signs of recent TCR signaling including high expression of *Zap70*, *Nfatc1*, and calcium influx pathway enrichment (cluster 7) (Figures 4D, 4E, and S5E, and S5F). Although Tox was

expressed by all Tex subsets (Figure 1C), Tex^{term} had the highest expression (Figures S5E and S5F). Gene-set enrichment analysis (GSEA) revealed that Tex^{prog1} and Tex^{prog2} shared similarity with $CXCR5^{+}Tim\text{-}3^{-}$ Tex cells and memory precursor effector cells (MPEC), although Tex^{prog1} had stronger enrichment (Figure 4G). Tex^{prog2} and Tex^{int} were enriched for signatures from circulating effectors (Tcirc) (Figure 4G). Tex^{int} and Tex^{term} enriched for the signature of $CXCR5^{-}Tim\text{-}3^{+}$ Tex cells, but Tex^{int} also showed similarity to short-lived effector cells (SLECs) (Figure 4G). Tex^{term} selectively enriched for exhaustion and resident-memory (Trm) signatures that coincided with elevated *Runx3*, a TF associated with tissue-residency (Figures 4G, S5E, and S5F) (Milner et al., 2017). Finally, each Tex subset enriched for transcriptional signatures of different populations of mouse and human TILs (Figure S5G). These transcriptional programs are consistent not only with a stepwise developmental program but also with acquisition of Tex subset-specific biological functions.

Distinct Epigenetic Remodeling and Associated TF Control of Tex Subsets

To define the epigenetic relationships between these Tex subsets, we next compared the open-chromatin landscape of the four Tex subsets, as well as Teff and Tmem cells, by assay for transposase-accessible chromatin followed by deep sequencing (ATAC-seq) (Buenrostro et al., 2013). Chromatin accessibility changes mostly occurred at intronic and intergenic regions and correlated with transcriptional changes of the nearest genes (Figures S6A and S6B). We identified specific patterns of chromatin accessibility in each Tex subset. For example, *Tcf7* and *Cxcr5* loci were more accessible in Tex^{prog1} and Tex^{prog2}, whereas *Cx3cr1* or *Cd38* had more accessibility in Tex^{int} or Tex^{term}, respectively (Figures 5A and S6C). By PCA, Tex^{prog1} and Tex^{prog2} were similar, whereas Tex^{int} and Tex^{term} were distinct from each other and also from either Tex^{prog} subset (Figure 5B). Each Tex subset also differed epigenetically from Teff and Tmem cells (Figures 5C, S6D, and S6E). Although Tex^{int} cells mapped closer to Teff and Tmem cells, this Tex subset remained distinct from Teff and Tmem by ≈ 5,000 open chromatin regions (OCRs) (including OCRs near *Tox* and *Pdcd1*). Many of these Tex^{int} OCRs or specific modules were also shared by other Tex subsets (Figures S6F and S6G; Table S4). Unsupervised clustering revealed five epigenetically distinct clusters between Tex subsets (Figure 5D; Table S5). Cluster 1 identified a set of OCRs uniquely shared between Tex^{prog1} and Tex^{prog2}. Many OCRs in this cluster mapped near genes related to progenitor biology (i.e., *Il2*, *Lef1*, *Wnt2*) (Table S5). Tex^{prog1} and Tex^{prog2} also enriched for cluster 2 that overlapped with Tex^{term} and cluster 4 associated with Tex^{int}. Tex^{prog2} showed more accessibility than Tex^{prog1} in cluster 5, a cluster also associated with Tex^{int} cells that contained OCRs associated with *mKi67* (Figure 5D; Table S5). Cluster 3, absent from either Tex^{prog} subset, was highly biased to Tex^{term} with some features moderately enriched in Tex^{int}. Overall, these open-chromatin landscapes highlighted an epigenetic similarity between Tex^{prog1} and Tex^{prog2} but also reveal aspects of Tex^{prog2} that were intermediate between Tex^{prog1} and Tex^{int}. However, robust epigenetic remodeling occurred during the Tex^{prog2} to Tex^{int} and Tex^{int} to Tex^{term} transitions (Figure 5E; Table S6). Most of the chromatin regions either opening or closing during the Tex^{int} to Tex^{term} transition occurred at sites that were unaffected during Tex^{prog2} to Tex^{int} differentiation and vice versa. Genes related to the progenitor biology (*Tcf7*, *Il7r*) were epigenetically silenced during the Tex^{prog2} to Tex^{int} transition and remained closed thereafter (Figure 5F; Table S6). Conversely, OCRs in genes encoding effector- (*Cx3cr1*)

and exhaustion-related genes (*Cd160*, *Nr4a* family members) became, respectively, less or more accessible during the Tex^{int} to Tex^{term} transition. Thus, a clear set of epigenetic landscape changes accompanied transitions between Tex subsets.

We next examined enrichment for TF binding sequences in chromatin accessible regions altered during Tex subset transitions using HOMER. These analyses identified TFs with potential subset-specific roles (Figure 5G; Table S7). For example, the most significantly enriched DNA binding sequence in chromatin differentially accessible in Tex^{prog2} versus Tex^{int} cells was for T cell factor family of TFs (e.g., *Tcf7*; TCF4 and TCF7L2 motifs) (Figure 5G left plot; Table S7). TF binding motifs enriched in Tex^{int} compared to Tex^{prog2} included ETS:RUNX (*Pu.1*, *Etv1*, *Etv2*, *Etv6*) and PRDM14 (*Znf264* and *Rfx7*). T-box motifs (e.g., Tbet, TBX2) were highly enriched in Tex^{int} compared to in Tex^{prog2} or Tex^{term} (Figure 5G; Table S7). Tex^{term}-specific OCRs were enriched for interferon-related TF motifs including the IRF1 sequence that can be bound by IRF1, IRF2, and IRF7 as well as sequences bound by STAT1 and Blimp-1. Combining motif enrichment analysis with RNA expression refined the list of TFs predicted to have Tex subset-specific roles. TCF1 (*Tcf7*) was the top-enriched TF in Tex^{prog2} (Figure 5H, left), whereas T-bet (*Tbx21*) was the most enriched for Tex^{int} (Figure 5H). Nr4a2 was the most-enriched predicted TF for the Tex^{term} subset, followed by Irf1, Nfatc1, and Eomes (Figure 5H). In the comparison of Tex^{prog2} to Tex^{int}, the enrichment for T-bet versus TCF1 was strongly anti-correlated, and these TFs displayed opposing protein-expression kinetics during the Tex^{prog2} to Tex^{int} transition (Figures 5H and 5I). Together, these data demonstrate *de novo* epigenetic changes occurring during the Tex^{prog2} to Tex^{int} and Tex^{int} to Tex^{term} transitions that coincided with gain or loss of accessibility for key TFs including potential opposing functions for TCF1 and T-bet in the Tex^{prog2} to Tex^{int} transition.

T-bet and TCF1 Control the Developmental Transition from Tex^{prog2} to Tex^{int} Cells

We next directly tested the impact of TCF1 and T-bet on Tex subset development. Co-adoptive transfer of naive P14 WT and P14 TCF1 cKO cells into LCMV-clone-13-infected mice revealed an essential role for TCF1 in early development of Tex^{prog1} and Tex^{prog2} cells (Figures 6A, 6B, and S7A-S7C) (Chen et al., 2019; Im et al., 2016; Utzschneider et al., 2016; Wu et al., 2016). TCF1-deficient P14 cells had almost exclusively a Tex^{int} phenotype at d8pi, although these cells were not maintained over time (Figures 6B and S7B). In the absence of T-bet (Figures S7D and S7E), there was a modest increase in the Tex^{prog1} subset at d8pi but marked reduction of the Tex^{int} population and accumulation of Tex^{term} cells (Figures 6C and 6D). At d15pi the loss of Tex^{int} cells was even more prominent, but the accumulation of Tex^{term} was lost (Figures 6E, 6F, and S7H). Consistent with previous reports (Kao et al., 2011; Paley et al., 2012), the number of all Tex cells was decreased in the absence of T-bet (Figures S7F, S7G and S7I), although there was a bias of T-bet cKO P14 cells toward the Tex^{prog1} and Tex^{prog2} compartments at d15pi (Figures 6E and 6F). These data identified a crucial role for T-bet specifically in the Tex^{int} subset. The higher frequency of Tex^{term} at d8pi in P14 T-bet cKO suggested that T-bet could stabilize the Tex^{int} stage, restraining conversion into Tex^{term} cells (Figures 6C and 6D), although there is likely also a role for T-bet in the non-exhausted $KLRG1^{+}$ Teff lineage at these early time points of infection (Chen et al., 2019). The inability to sustain the development of the Tex^{term}

population at d15pi in the T-bet cKO likely reflected a lack of replenishment caused by defective generation of Tex^{int} cells from Tex^{prog2} (Figures 6C-6F and S7H). Thus, the defect in Tex^{int} cell development in the absence of T-bet disrupted Tex subset dynamics, causing attrition of the overall $CD8^+$ T cell response during chronic infection.

To confirm these results, we enforced expression of either TCF1 (short isoform) or T-bet in P14 $CD8^+$ T cells with retroviral (RV) transduction (Kurachi et al., 2017) (Figure S7J). TCF1 overexpression (VEX+) favored accumulation of Tex^{prog1} and Tex^{prog2} at d15pi, reducing the proportion of Tex^{int} and Tex^{term} cells in comparison with the non-transduced (VEX–) or empty RV controls (Figures 6G and S7K). Conversely, enforcing T-bet expression led to a substantial accumulation of Tex^{int} cells, whereas the proportion of Tex^{prog1}, Tex^{prog2}, and also Tex^{term} cells was reduced (Figures 6G and S7K). These data further illustrated the role of T-bet in fostering and stabilizing the Tex^{int} subset. Taken together, we defined the TCF1-T-bet axis as a major transcriptional control mechanism in the conversion of progenitor cells into Tex^{int} cells.

The High-Mobility Group (HMG) Box Protein TOX Antagonizes T-bet Expression to Favor Terminal Exhaustion

We next aimed to investigate the molecular events promoting final conversion of Tex^{int} cells to terminal Tex^{term} cells. We and others recently reported a role for Tox in early Tex versus Teff cell-fate commitment (Alfei et al., 2019; Khan et al., 2019; Scott et al., 2019; Seo et al., 2019; Yao et al., 2019). We then asked whether Tox might antagonize the T-bet-driven Teff-like Tex^{int} subset to favor terminal exhaustion. Indeed, Tox expression was lowest in Tex^{int} cells but increased robustly at the Tex^{term} stage (Figures 7A, S5E, and S5F). Tex^{int} cells also had the lowest Tox/T-bet ratio. Moreover, when examined directly, the Tox and T-bet co-expression pattern revealed distinct Tox^{hi}T-bet^{lo} and Tox^{int}T-bet^{hi} populations at d27pi (Figure 7B). Accordingly, in chronic infection and cancer, lower Tox was characteristic of T-bet^{hi} Tex^{int} cells whereas higher Tox was associated with Tex^{term} and/or Tex^{prog} subsets that were T-bet^{lo} (Figures 7C-7F). Tox also had a predictive binding site at an OCR distal to the *Tbx21* TSS, and among all TFs predicted to bind near *Tbx21* in Tex cells, Tox was among the most anti-correlated with *Tbx21* mRNA (Figures 7G and 7H). These data suggested potential direct negative regulation of T-bet by Tox.

To test this relationship, we performed co-transfer of Tox haplo-insufficient P14 cells ($Tox^{+/-}$) with WT littermate ($Tox^{+/+}$) in congenic mice followed by clone-13 infection (Figure 7I). $Tox^{+/-}$ P14 cells had ~20%–30% reduction in Tox expression (Figure 7K, bottom) in ~60% of the recipient mice by d27pi. Whereas a complete abrogation of Tox precludes Tex cell development (Alfei et al., 2019; Khan et al., 2019; Scott et al., 2019; Seo et al., 2019; Yao et al., 2019), $Tox^{+/-}$ P14 cells expanded normally, were maintained up to d27pi (although at reduced frequencies and numbers compared to $Tox^{+/+}$ P14 cells), and sustained high expression of PD-1 consistent with exhaustion (Figures 7J, 7K left, and S7L). However, tempering Tox expression reduced the Tex^{prog1}, Tex^{prog2}, and Tex^{term} compartments and favored accumulation of Tex^{int} cells (Figure 7K). Although the absolute number of all Tex subsets was reduced in the $Tox^{+/-}$ setting, the Tex^{int} cells were affected the least (Figure 7L). These data confirmed a developmental advantage for Tex^{int} cells in

$Tox^{+/-}$ P14 that corresponded to an overall increase in T-bet expression in comparison with $Tox^{+/+}$ P14 controls, a difference also apparent in the Tex^{int} subset (Figure 7M). These data indicated that Tox control over T-bet expression in Tex cells represents a key switch point regulating the balance between Tex^{int} and Tex^{term} cell accumulation.

DISCUSSION

We and others have previously identified Tex subsets. However, the number of subsets, their underlying transcriptional and epigenetic control, and their developmental relationships have remained poorly understood. Here, we identified a four-stage developmental trajectory of Tex cell subsets defined by Ly108 (a surrogate of TCF1) and CD69. Our data revealed two interchangeable progenitor states (Tex^{prog1} and Tex^{prog2}) with transcriptional, phenotypic, functional, and anatomical differences but a related open-chromatin landscape. Tex^{prog1} are quiescent and resident and convert to Tex^{prog2}. This conversion was associated with relocalization from blood-inaccessible lymphoid residence to blood-accessible locations and a proliferation-driven transition to a downstream Tex^{int} developmental stage. This Tex^{int} subset had similarities to circulating “effector-like” cells, although Tex^{int} cells were epigenetically distinct from bona fide Teff cells. Tex^{int} cells ultimately converted to Tex^{term} cells that were absent from the blood but accumulated in tissues and the blood-accessible locations in the spleen. We also discovered a TF cascade as Tex cells transitioned from $TCF1^{hi}Tox^{hi}$ to $TCF1^{int}Tox^{hi}$ to $TCF1^{neg}T\text{-}bet^{hi}Tox^{int}$ and finally to $TCF1^{neg}T\text{-}bet^{lo}Tox^{hi}Eomes^{hi}$ during Tex subset conversion. Moreover, we defined key roles for these TFs in this developmental trajectory, although other TFs likely also have a role. These findings also reconcile previous differences between descriptions of Tex subsets that could have related to whether the $T\text{-}bet^{hi}$ Tex^{int} subset was included in a progenitor or terminal population in earlier two subset models (Im et al., 2016; Paley et al., 2012; Utzschneider et al., 2016). Moreover, although there will likely be disease-specific features, the general biology identified here appears to be preserved across diseases and species, suggesting a conserved core developmental biology.

These studies also provided additional insights about the biological role of T-bet in Tex cells. First, T-bet drove conversion of $TCF1^{+}$ progenitor Tex cells to $TCF1^{-}$ Tex^{int} cells. Second, the Tex^{int} subset re-engaged some effector-like activity and migration reminiscent of T-bet functions in other $CD8^{+}$ T cells (Berrien-Elliott et al., 2015; Intlekofer et al., 2008; Intlekofer et al., 2005; Pearce et al., 2003; Taqueti et al., 2006). Third, T-bet stabilized the Tex^{int} stage, preventing terminal exhaustion, whereas this activity was counterbalanced by Tox. Moreover, two recent studies highlight a $CX3CR1^{+}$ Tex subset that possesses an effector-like transcriptional program, expresses T-bet, and is similar to the Tex^{int} subset defined here (Hudson et al., 2019; Zander et al., 2019). Together, these data highlight additional functions for T-bet as a central coordinator of an intermediate Tex subset and identify the TCF1, T-bet, and Tox axes as essential components regulating the development and balance between Tex subsets.

PD-1 pathway blockade preferentially amplifies the Tex subsets with circulatory potential (i.e., Tex^{prog2} and Tex^{int} cells) consistent with detection of responses in the blood after PD-1 blockade in cancer patients (Huang et al., 2017). The observed Increase in effector-

like transcriptional features in the Tex^{int} subset despite a Tex cell epigenetic landscape Is consistent with reengagement of effector gene transcription but lack of epigenetic changes associated with PD-1 pathway blockade (Pauken et al., 2016). Because Tex^{int} cells also convert to Tex^{term}, these data also predict a potential replacement of Tex^{term} in tumors with new Tex^{int} converting to Tex^{term} cells after PD-1 blockade consistent with accumulation of $Eomes^{hi}$ Tex cells after blockade or loss of PD-1 (Huang et al., 2017; Odorizzi et al., 2015; Pauken et al., 2016). Moreover, these dynamics could explain the clonal replacement observed in humans after PD-1 blockade (Yost et al., 2019). T-bet directly represses PD-1 in Tex cells (Kao et al., 2011), and we consistently observed a modest decrease in PD-1 expression in the $Tex^{prog1} \rightarrow Tex^{prog2}$ and $Tex^{prog2} \rightarrow Tex^{int}$ transitions. Thus, it is possible that by restraining antigen-dependent TCR signals, PD-1 protects Tex progenitors. A subtle transient downregulation of PD-1 by T-bet, and therefore increase In TCR and/or costimulatory signaling, could provoke loss of TCF1, re-entry to cell cycle, and differentiation to Tex^{int}, although whether loss of TCF1 instigates T-bet expression or vice versa remains currently unclear. Blocking PD-1 signals could provoke a similar effect, causing a synchronous and robust conversion of Tex^{prog2} into Tex^{int}.

These observations also have relevance for understanding Tex biology in humans with chronic viral infections and cancers. For example, CyTOF analysis in patients with HIV or non-small-cell lung cancer identified 9 clusters of Tex cells that expressed IRs and Tox (Bengsch et al., 2018). One rare cluster in the blood was $TCF1^{+}$, $PD\text{-}1^{+}$, and $CXCR5^{+}$, which was associated with less severe disease and might represent Tex^{prog1}-like cells (Bengsch et al., 2018). Several other clusters expressed lower TCF1 and/or lacked CXCR5 and were $Ki67^{+}$ bearing resemblance to Tex^{prog2}. Three additional clusters resembled Tex^{int}, expressing T-bet, Ki67, and/or cytotoxicity molecules. Finally, two clusters were more similar to Tex^{term} or Tex^{int} just transitioning to Tex^{term} and had high Tox, IRs, and Eomes and lacked Ki67. Notably, some of these latter clusters correlated with more severe disease and/or were enriched in lung tumors in comparison with blood (Bengsch et al., 2018). In addition, other studies in humans identified cells similar to Tex^{prog1} in lymphoid aggregates in tumors (Jansen et al., 2019), proliferating in the peripheral blood after checkpoint blockade similar to Tex^{prog2} and/or Tex^{int} (Huang et al., 2019; Huang et al., 2017; Kamphorst et al., 2017) or clonally related populations in tumors with features of Tex^{prog} cells and Tex^{int} or Tex^{term} (Li et al., 2019; Wu et al., 2020; Zhang et al., 2018) consistent with the lineage relationships defined here.

Most tissues are organized into proliferative hierarchies, and these hierarchies are important in settings of proliferative stress (Grompe, 2012). Often, these regenerative hierarchies involve a quiescent tissue stem cell or progenitor cell that could receive local tissue signals, for example the crypt base columnar cell or hematopoietic stem cell (Gehart and Clevers, 2019; McCracken et al., 2016). There is often also a second progenitor population that can display more steady-state cell cycle (Grompe, 2012; McCracken et al., 2016). In some settings these two progenitor populations could interconvert, especially if proliferative stress is increased (Grompe, 2012). In these tissues there is often also a transient amplifying population that is more numerically abundant and occupies that part of the developmental hierarchy where most proliferation has occurred, but also where cells acquire major biological features of the function of the tissue. Finally, terminally differentiated tissue cells

are formed. Although these cells, such as post-mitotic intestinal enterocytes (Gehart and Clevers, 2019; Grompe, 2012), are terminally differentiated, they are critical for the function of the tissue. Each step in these tissue proliferative hierarchies, which allow cells to manage proliferative stress and regeneration, has possible analogies to Tex cell biology including two distinct but interconvertible progenitor populations: a transient amplifying population that acquires key functions of the tissue and a terminal population that is short-lived, but likely has key biological functions. In some of these settings, the proliferative hierarchy has branches allowing different types of more differentiated descendant cells to be formed (Gehart and Clevers, 2019; McCracken et al., 2016). Whether the Tex cells proliferative hierarchy contains more complexity than revealed here remains to be determined.

Together, these studies help clarify our understanding of Tex subset heterogeneity as well as define the biological properties and associated underlying transcriptional and epigenetic control of Tex cell heterogeneity. These “maps” of Tex cell biology could allow more detailed understanding of data from cancer patients to determine which aspects of Tex cells have been altered by therapeutic interventions. Finally, these data also illustrate a developmental biology structure for Tex cell differentiation and highlight similarities to other biological settings where a hierarchy of progenitor cell maintenance and differentiation balances proliferative stress and homeostatic functions of the “tissue.”

STAR★METHODS

RESOURCE AVAILABILITY

Lead Contact—Further information, requests for resources and reagents should be directed to the lead contact, E. John Wherry (wherry@pennmedicine.upenn.edu).

Materials Availability—Materials generated by this study are available upon request.

Data and Code Availability—The accession number for the RNAseq and ATACseq reported in this paper is GEO:GSE149879.

EXPERIMENTAL MODEL AND SUBJECT DETAILS

Patients samples—Results presented in this study were obtained by re-analyzing tumor resection data from clinical stage III or stage IV melanoma patients involved in a previously reported clinical trial at the University of Pennsylvania (NCT02434354) (Huang et al., 2019) or collected from patients under IRB protocol 08607 at the University of Pennsylvania. Flow cytometry and staining were performed as previously described. (Huang et al., 2019) Samples were collected either before or 3 weeks after treatment with a single flat dose of pembrolizumab 200mg intravenously. The protocol and its amendments were approved by the Institutional Review Board at the University of Pennsylvania, and all patients provided written informed consent.

Mice—Six-week old female C57BL/6 mice (CD45.2, Charles River, NCI) were used for most experiments. Alternatively, six-week old female NCI B6-Ly5.1/Cr (NCI Charles River) or male B6.SJL-Ptprc Pepc/BoyJ mice (The Jackson laboratory) expressing the congenic marker CD45.1 were used as recipients for some P14 knockout adoptive transfers and CFSE

tracing experiments. P14 TCR transgenic mice expressing a TCR specific for the LCMV D^bgp33-41 peptide were bred in house and backcrossed onto the C57BL/6 background. P14 *Tcf7*$^{flox/flox}$ CD4-cre (P14TCF1KO) mice were bred in house by crossing CD4-cre mice (The Jackson laboratory) to *Tcf7*$^{flox/flox}$ mice on the P14 background. *Tbx21*$^{flox/flox}$ from the Jackson Laboratory (B6.128-Tbx21tm2Srnr/J) were bred in house with P14 ERT2-Cre$^{+/-}$ Rosa26-YFP$^{+/-}$ to generate P14 *Tbx21*$^{flox/flox}$ ERT2-CRE$^{+/-}$ Rosa-YFP$^{+/-}$ mice (P14TbetKO). *Tox*^{KO} mice were kindly provided by Jonathan Kaye, PhD (Cedars-Sinai Medical Center, Los Angeles, CA, USA) and bred in house onto the P14 background to generate P14 *Tox*$^{+/-}$ mice. All experiments and breeding conditions were in accordance with Institutional Animal Care and Use Committee (IACUC) guidelines for the University of Pennsylvania.

Viruses and Infections—LCMV Armstrong and clone 13 were grown in BHK cells and titrated using plaque assay on VERO cells. Recipient mice were infected either intraperitoneally (i.p.) with LCMV Armstrong ($2x10^5$ plaque forming units [PFU]) or intravenously (i.v.) with LCMV clone 13 ($4x10^6$ PFU) one day post adoptive transfer of P14 cells where noted.

Cell line and tumor transplant—B16 and MC-38 tumor cells were maintained in DMEM supplemented with 10% FCS, 1% L-glut and 1% Pen/Strep. Tumor cells ($5x10^5$) cultured for less than two weeks were implanted subcutaneously in the flank of recipient mice using 29G1/2 syringes. Tumor size was monitored using a manual caliper and tumors were excised before exceeding the volume permitted by the IACUC guidelines for the University of Pennsylvania.

Retroviral vectors—*Tbx21* and *Tcf7* short isoform (p33; Origene) cDNAs were cloned into a MSCV-IRES-VEX plasmid. Retroviral particles were produced by transfection of 293T cells. Briefly, 293T cells were pre-incubated with warmed cDMEM supplemented with chloroquine (25μM; Sigma). Cells were transduced with a pCL-Eco plasmid (15μg) and MSCV-IRES-VEX expression plasmid (15μg) using Lipofectamine 3000 (ThermoFisher Scientific) for 6 h at 37°C 5%CO2. After incubation, transduction medium was replaced with fresh cDMEM. RV supernatant were collected at days 3 and 4 of culture and titrated on NIH 3T3 cells.

METHODS DETAILS

Adoptive T cell transfer—Recipient mice were adoptively transferred with PBMCs containing $1x10^3$ P14 CD8$^+$ T cells 24 h prior infection with either LCMV Armstrong or LCMV clone 13. P14TCF1KO (CD45.1.2$^+$) or P14 TOX$^{+/-}$ (CD45.2$^+$) were co-transferred along with their relative WT P14 littermate controls (CD4-Cre$^+$ *Tcf7*$^{+/+}$ [CD45.1$^+$] or *Tox*$^{+/+}$ [CD45.1.2$^+$] respectively), $1x10^3$ each. For T-bet KO experiments, P14WT (ERT2-Cre$^{+/-}$ Rosa26-YFP$^{+/-}$ *Tbx21*$^{+/+}$; CD45.1.2$^+$) and P14TbetKO (ERT2-Cre$^{+/-}$ Rosa26 YFP$^{+/-}$ *Tbx21*$^{flox/flox}$, CD45.2$^+$) were treated *in vitro* with TAT-cre (50μg/mL) in serum free RPMI medium for 45min at 37°C, 5%CO2 and $1x10^3$ of each were co-transferred into naive CD45.1 recipients 24 h before infection. (Gordon et al., 2012) Markers typically associated

with early T cell activation (i.e., CD69, Ly6C, PD-1, CD25, CD62L, CD127) were checked in each P14 populations before infusion into recipient mice to ensure transfer of naive cells.

Cell preparation, flow cytometry and cell sorting—Spleens and inguinal lymph nodes (LN) were mechanically disrupted onto a 70μM cell strainer using the plunger of a 3mL syringe and resuspended in 1mL of ACK red blood cell lysing buffer (GIBCO) for 3 min at room temperature (RT). Cell suspensions were washed in cRPMI supplemented with 10% FBS, 1% penn/strep, 1% L-glut, HEPES 10mM (Cell Center, UPenn), MEM non-essential amino acids 1% (GIBCO), Sodium Pyruvate 1mM (Cell Center Upenn), β-mercaptoethanol (0.05mM) and resuspended in FACs buffer (PBS1%, 1%FBS, EDTA [2mM]). Bone marrow suspensions were harvested by flushing cells out of the femur and tibia of infected mice with a 29G syringe and cRPMI. Cells were then treated as above. For lungs and livers, mice were perfused with cold PBS to maximize removal of blood stream cells from organs. Lungs were cut in a Petri dish, disrupted in the presence of Collagenase D (1X) (Roche) using a MACs dissociator (Miltenyi Biotec) and incubated for 45min at 37°C under agitation. After incubation, lung cells were disrupted a second time on a MACs dissociator (Miltenyi Biotec) and processed as above. After mechanical disruption onto a 70μM strainer, lymphocytes from livers were enriched using Percoll (GE Healthcare) density gradient separation (80%/40%), washed two times with cRPMI and processed as above. Blood samples were collected in 1ml of PBS plus 2mM EDTA. RPMI was added and samples were underlaid with Histopaque 1083 (Sigma Aldrich) for lymphocyte enrichment using density gradient concentration. Remaining red blood cells were lysed using ACK lysing buffer (GIBCO) for 3min at RT. For enrichment of mouse TILs, tumors were cut in pieces using a scalpel and incubated in serum free RPMI containing Collagenase D Type 4 (1mg/mL, Worthington) and 0.02mg/mL of DNase I (Sigma) 45 min at 37°C under agitation. Cell suspensions were filtered again on a 70μM strainer and processed as above (Ngiow et al., 2016). Equal number of cells were stained with extracellular antibodies for 30min on ice in FACs buffer (PBS1X, 1%FBS, 2mMEDTA) in the presence of Live/Dead Fixable Aqua Cell Stain (ThermoFisher Scientific). For tumor samples staining, anti-mouse CD16/32 (Biolegend) was added (1/100) at the time of extra-cellular staining as previously described. (Muroyama et al., 2017) Cells were then fixed for 20 min on ice with Cytofix/Cytoperm (BD bioscience) for intracellular proteins detection (active-caspase3, granzyme B, IFNγ, TNFα), incubated 30 min on ice in Perm/Wash buffer (BD bioscience) and stained for an extended 1 h on ice in Perm/Wash buffer (BD bioscience) containing antibodies for intracellular proteins. For TFs detection, cells were fixed and permeabilized using the Foxp3 Transcription Factor buffer set (ThermoFisher Scientific) and incubated for an additional 1 h with TF antibodies. Samples were acquired on an LSR II or BD FACSymphony and analyzed with FlowJo v.10 software (Tree Star Inc).

For cell sorting, $CD8^+$ T cells were enriched from total splenocytes using the EasySep^{tm} $CD8^+$ T cell isolation Kit (StemCell) (routinely > 90% purity). $CD8^+$ T cells were stained with Live/Dead Fixable Aqua Cell Stain (ThermoFisher Scientific) and Tex subsets were sorted based on CD8, CD45.1, CD45.2, CD69 and Ly108 for *in vitro* CFSE proliferation assays, killing assays, RNaseq and ATACseq experiments. For *in vivo* CFSE tracing, Tex subsets were sorted from activated $CD8^+$ T cells using CD4 and CD19 as exclusion markers

and PD-1 to gate on activated cells and CD69 and Ly108 to identify each Tex subset. Cells were sorted on an BD FACSARIA (BD Bioscience) using a 70 micron nozzle in RPMI 50%FBS maintained at 4°C using a circulating cool-down system. Purity was routinely > 94%.

Intracellular cytokine staining—Splenocytes (1-2x10^6) were re-stimulated *in vitro* for 5 h at 37°C 5% CO2 in cRPMI supplemented with GolgiStop (1/250; BD bioscience), GolgiPlug (1/500; BD bioscience), gp_{33-41} peptide (NIH, 0.4μg/mL) and CD107a antibodies (1/500). Cells were then washed and stained using the BD Fixation/permeabilization kit (BD Bioscience).

CFSE tracing experiments—C57BL/6 mice ($CD45.2^+$) were infected with LCMV clone 13 and spleens were collected at day 21 pi. Mice with low viral titers in the serum at day 15pi were excluded. $CD8^+$ T cells were enriched using EasySep^{tm} $CD8^+$ T cell isolation Kit (StemCell) (routinely > 90% purity) and Tex subsets were sorted from endogenous activated $CD8^+$ T cells. Briefly, Live/Dead Fixable Aqua Cell Stain (ThermoFisher Scientific), CD4 and CD19 were used as exclusion markers and PD-1, Ly108 and CD69 were used to discriminate and sort Tex subsets among endogenous activated ($PD\text{-}1^+$) $CD8^+$ T cells (purity was routinely > 94% for each subset). Sorted cells were stained with Carboxyfluorescein succinimidyl ester (CFSE; ThermoFisher Scientific) for 8min at RT in PBS containing the CFSE dye (5μM). Reaction was stopped by adding an equal volume of cold FBS and cells were subsequently washed two times in cRPMI. Cells were counted and 1x10^5 of each subset was adoptively transferred into infection-matched $CD45.1^+$ recipient mice. Proliferation and phenotypic changes were assessed in the spleen seven days post-transfer.

Intravascular staining—Intravascular staining was performed as previously described. (Anderson et al., 2014) At day 30 pi, recipient mice were injected i.v. with 200μl of PBS containing 3μg of eF-450-conjugated anti-CD8 antibody (ThermoFisher Scientific). Three minutes later, mice were sacrificed and spleens were collected and processed as above.

Antibody treatment—Where indicated, mice were depleted of $CD4^+$ T cells using two i.p. injections of 200μL of PBS containing 200μg of monoclonal anti-CD4 antibody (clone GK1.5, BioXcell) one day prior and post infection with LCMV clone 13.

PD-L1 blockade was performed in CD4-depleted mice as previously described. (Pauken et al., 2016) Sequential i.p. injections of 200μl of PBS containing or not rat anti-mouse PD-L1 monoclonal antibody (200μg/injection, clone 10F.9G2, BioXcell) were performed every three days between days 22 and 34 for a total of five injections.

CFSE Proliferation assay *in vitro*—*In vitro* CFSE proliferation assays were performed as previously described (Beltra et al., 2016). Sorted Tex subsets were re-suspended in 1ml of PBS and stained for 6min with CFSE by addition of an equal volume of PBS containing 4μM of CFSE (2μM final). The reaction was stopped by addition of an equal volume of cold FBS and cells were subsequently washed two times in cRPMI. Dendritic cells (DCs) were enriched from the spleen of naive C57B/L6 mice using CD11c+ MicroBeads Ultra pure mouse kit (Miltenyi) and loaded with gp_{33-41} peptide (0.1 μM) for 30min at 37°C 5% CO2

in cRPMI. Each Tex subset was co-cultured with peptide loaded DCs (10^4 each) for three days in 96-round bottom well plates.

Killing assay—Splenocytes from naive CD45.2$^+$ C57BL/6 mice were coated with 0.2μM of gp_{33-41} peptide (targets) or the irrelevant $OVA_{257-264}$ SIINFEKL peptide (non-target). Target and non-target cells were stained with CFSE at 0.1 and 10μM respectively. Target and non-target cells were incubated or not with sorted Tex subsets (E:T 3/1) for 16 h in cRPMI. Percentage of specific lysis was calculated as follows: 100-((100X % gp33 targets)/% gp33 targets without effectors).

Retroviral (RV) transduction—RV transduction of P14 CD8$^+$ T cells was performed as described (Kurachi et al., 2017). P14 CD8$^+$ T cells were enriched from total splenocytes using EasySep^{tm} CD8$^+$ T cell isolation Kit (StemCell) and activated *in vitro* in cRPMI supplemented with αCD3 (1 μg/mL), αCD28 (0.5μg/mL) antibodies and IL-2 (100U/mL) (PeproTech). One day post activation (between 24-27 h), activated CD8$^+$ T cells were enriched using Percoll (GE Healthcare) density gradient (30%/60%) and spin-transduced during 60-75min at *2000*g 30°C with RV supernatant containing polybrene (4μg/mL). Transduced cells were then incubated for 6 h, washed twice in cRPMI, counted and injected ($1x10^5$ per mouse) into LCMV clone 13 infected mice at day 1.5pi.

Active caspase-3 detection—Splenocytes from infected mice or TILs isolated from Human melanoma tumors were incubated for 5 h at 37°C 5%CO2 in cRPMI prior intra-cytoplasmic detection of active-caspase 3 (BD Bioscience) using BD Fixation/ Permeabilization kit (BD Bioscience).

Sample preparation for RNaseq—Sorted cells were centrifuged, resuspended in 350μl of RLT buffer (RNeasy Plus Micro kit, QIAGEN) in DNA LoBind tubes (Eppendorf), vortexed for 30 s, flash-frozen on dry ice and stored at −80°C. mRNA was extracted using RNeasy Plus Micro kit (QIAGEN) following manufacturer's protocol and eluted in 14μl of RNase free water. mRNA quality was assessed on a 2200 TapeStation (Agilent Technologies) using High Sensitivity RNA ScreenTape (Agilent Technologies). mRNA from each biological replicate (5ng/sample) was converted into cDNA and amplified (9 cycles) using the SMART-Seq V4 Ultra Low Input RNA Kit (Takara Bio). 10ng of cDNA was used to prepare DNA libraries using Nextera XT DNA Library Prep Kit (Illumina). Barcoded samples were pooled, diluted at 1.8pM, loaded onto a TG NextSeq 500/550 High Output Kit v2 (150 cycles, 400M reads, Illumina) and paired-end sequencing was performed on a NextSeq 550 (Illumina).

Sample preparation for ATACseq—ATACseq sample preparation was performed as described with minor modifications. (Buenrostro et al., 2013) Sorted cells ($2.5\text{-to-}5x10^4$) were washed twice in cold PBS and resuspended in 50μl of cold lysis buffer (10nM Tris-HCl, pH 7.4, 10mM NaCl, 3mM MgCl2, 0.1% Tween). Lysates were centrifuge (750xg, 10min, 4°C) and nuclei were resuspended in 50μl of transposition reaction mix (TD buffer [25μl], Tn5 Transposase [2.5μl], nuclease-free water [22.5μl]; (Illumina)) and incubated for 30min at 37°C. Transposed DNA fragments were purified using a QIAGEN Reaction MiniElute Kit, barcoded with NEXTERA dual indexes (Illumina) and amplified by PCR for

11 cycles using NEBNext High Fidelity 2x PCR Master Mix (New England Biolabs). PCR products were purified using a PCR Purification Kit (QIAGEN) and amplified fragments size was verified on a 2200 TapeStation (Agilent Technologies) using High Sensitivity D1000 ScreenTapes (Agilent Technologies). Libraries were quantified by qPCR using a KAPA Library Quant Kit (KAPA Biosystems). Normalized libraries were pooled, diluted to 1.8pg/mL loaded onto a TG NextSeq 500/550 High Output Kit v2 (150 cycles, 400M reads, Illumina) and paired-end sequencing was performed on a NextSeq 550 (Illumina).

QUANTIFICATION AND STATISTICAL ANALYSIS

Spice charts analysis—Positive gates for each parameter were created in FlowJo (V10.4.2, Tree Star) and the Boolean tool was used to evaluate the frequency of cells in each possible combination of markers for each sample of interest. Excel sheet containing all the samples and relative frequencies of cells in each combination was created from FlowJo, converted to a spice-compatible file using Pestle and pie charts were realized with Spice (v5.35).

RNA seq—Raw FASTQ files from RNaseq paired-end sequencing were aligned to the GRCm38/mm10 reference genome using Kallisto (https://pachterlab.github.io/kallisto/), filtered to remove transcripts with low counts and trimmed using the TMM normalization method. Genes with differential expression across samples (DEGs) were assessed using the Limma package of R. A FDR of 0.01 and Log2 fold change cut-off of 1 were imposed. PCA plots were built using normalized and filtered $\log_2$ cpm. Unsupervised clustering was performed using K-means to cluster heatmap rows. ComBat in the R package svaseq was used to correct for non-biological variations accounting for unwanted differences when merging the RNaseq dataset from this paper and the Scott-Browne et al. (2016) (Scott-Browne et al., 2016) RNaseq dataset for comparisons. (Leek, 2014)

Gene ontology—Gene ontology of gene sets of interest were obtained using the Metascape online tool (http://metascape.org/gp/index.html#/main/step1). Pathway enrichment analysis (GO Biological processes) was set for a minimum overlap of 3, a *p-value* cut-off of 0.01 and a minimum enrichment score of 1.5. The five pathways with the most significant enrichment score by log (q-value) were presented and plotted onto a bubble graph using Datagraph (https://www.visualdatatools.com/DataGraph/).

Gene set enrichment analysis—GSEA was performed using the Broad Institute software (https://www.broadinstitute.org/gsea/index.jsp). Enrichment scores were calculated by comparing each Tex subset (Tex^{prog1}, Tex^{prog2}, Tex^{int} and Tex^{term}) to the three others. Multiple comparative analysis were performed using datasets publicly available through the Gene Expression Omnibus (GEO) database (https://www.ncbi.nlm.nih.gov/gds) under the following accession numbers: CXCR5+Tim3− and CXCR5−Tim3+ (GSE84105)(Im et al., 2016), MPEC and SLEC (GSE8678)(Joshi et al., 2007), state 1 (plastic) and state 2 (fixed) (GSE89307)(Philip et al., 2017) or using gene signatures listed as supplemental material: T_{RM} and T_{CIRC} (Milner et al., 2017), Texhausted (Bengsch et al., 2018), CD8-G, CD8-B and CD8-1_to_6.(Sade-Feldman et al., 2019)

ATACseq—Raw ATACseq FASTQ files from paired-end sequencing were processed using the script available at the following repository (https://github.com/wherrylab/jogiles_ATAC). DWe used samtools to remove unmapped, unpaired, mitochondrial reads and ENCODE blacklist regions were also removed (https://sites.google.com/site/anshulkundaje/projects/blacklists). PCR duplicates were removed using Picard. Peak calling was performed using MACS v2 (FDR q-value 0.01). For each experiment, we combined peaks of all samples to create a union peak list and merged overlapping peaks with BedTools *merge*. The number of reads in each peak was determined using BedTools *coverage*. Differentially accessible regions were identified following DESeq2 normalization using a FDR cut-off < 0.05 or 0.01 unless otherwise indicated. ComBat in the R package svaseq was used to correct for non-biological variations accounting for unwanted differences when merging the ATACseq dataset from this paper and the Pauken et al. (2016)(Pauken et al., 2016) ATACseq dataset for comparisons.(Leek, 2014)

Correlation network analysis—For all pairwise comparisons, a correlation coefficient was calculated using the Spearman method. A correlation network was created based on correlation scores and projected using Cytoscape.

Motif enrichment analysis—Motif enrichment was calculated using HOMER (default parameters) on peaks differentially accessible during indicated Tex subset transitions (Figure 5e; Table. S6). Transcription binding site prediction analysis was performed using the *de novo* motif discovery strategy. For each predicted motif, top 10 TF matches were selected and shown in Table. S7 and the top match was highlighted in Figure 5g.

Sample distance analysis—A distance matrix was calculated using the “euclidean” measure using the top 25% peak by variance and plotted as a heatmap in Figure S6E.

Biclustering analysis—Differential expression of genes was calculated for all pairwise comparisons of cell states using *DESeq2_1.22.2*. Normalized expression values of genes which are differential in any of the pairwise comparison were used as input to bicluster the data using the *SpectralBiclustering* method from the *scikit-learn_0.21.3* package. Seven gene modules were calculated for the four sample groups.

Gene signature analysis on scRNaseq data—The single cell expression data used was from *GSE122712* (https://www.ncbi.nlm.nih.gov/geo/query/acc.cgi?acc=GSE122712) (Miller et al., 2019), the supplementary files from the repository were used as input and processed using the *Seurat_3.1.1* package. The above-calculated seven gene modules were used as features to calculate module scores of single cells using the *AddModuleScore* function from the *Seurat_3.1.1* package. Module scores for each of the gene signatures was used to color the cells on the *UMAP* projection created from the *Seurat* processing.

Statistical analysis—Statistics on flow cytometry data were performed using unpaired two-tailed Student’s t test (GraphPad Prism v6; *p < 0.05, **p < 0.005, ***p < 0.0005).

Supplementary Material

Refer to Web version on PubMed Central for supplementary material.

ACKNOWLEDGMENTS

We thank the Wherry lab for input. This work was funded by NIH grants N2T32CA009615; CA230157 (A.C.H.); CA234842 (Z.C.); and AI105343, AI108545, AI117950, AI082630, and CA210944 (E.J.W.). This work was also supported by the Tara Miller Foundation (A.C.H.), the Melanoma Research Alliance (E.J.W.), the David and Hallee Adelman Immunotherapy Research Fund (E.J.W.), and the Parker Institute for Cancer Immunotherapy Bridge Scholar Award (A.C.H.). S.F.N. is supported by the NHMRC CJ Martin Fellowship GNT1111469 and the Mark Foundation for Cancer Research Momentum Fellowship. M.S.A.H. is a Cancer Research Institute (CRI) Irvington Postdoctoral fellows. J.R.G. is a Cancer Research Institute-Mark Foundation Fellow and was previously supported by T32CA009140. We thank the Human Immunology Core and the Tumor Tissue and Biospecimen Bank of the University of Pennsylvania (supported by P30-CA016520 and P50-CA174523). Work in the Wherry lab is supported by the Parker Institute for Cancer Immunotherapy.

REFERENCES

Alfei F, Kanev K, Hofmann M, Wu M, Ghoneim HE, Roelli P, Utzschneider DT, von Hoesslin M, Cullen JG, Fan Y, et al. (2019). TOX reinforces the phenotype and longevity of exhausted T cells in chronic viral infection. Nature 571, 265–269. [PubMed: 31207605]

Anderson KG, Mayer-Barber K, Sung H, Beura L, James BR, Taylor JJ, Qunaj L, Griffith TS, Vezys V, Barber DL, and Masopust D (2014). Intravascular staining for discrimination of vascular and tissue leukocytes. Nat. Protoc 9, 209–222. [PubMed: 24385150]

Beltra JC, Bourbonnais S, Bédard N, Charpentier T, Boulangé M, Michaud E, Boufaied I, Bruneau J, Shoukry NH, Lamarre A, and Decaluwe H (2016). IL2Rβ-dependent signals drive terminal exhaustion and suppress memory development during chronic viral infection. Proc. Natl. Acad. Sci. USA 113, E5444–E5453. [PubMed: 27573835]

Bengsch B, Ohtani T, Khan O, Setty M, Manne S, O'Brien S, Gherardini PF, Herati RS, Huang AC, Chang KM, et al. (2018). Epigenomic-Guided Mass Cytometry Profiling Reveals Disease-Specific Features of Exhausted CD8 T Cells. Immunity 48, 1029–1045.e5, e1025. [PubMed: 29768164]

Berrien-Elliott MM, Yuan J, Swier LE, Jackson SR, Chen CL, Donlin MJ, and Teague RM (2015). Checkpoint blockade immunotherapy relies on T-bet but not Eomes to induce effector function in tumor-infiltrating CD8+ T cells. Cancer Immunol. Res 3, 116–124. [PubMed: 25516478]

Beura LK, Anderson KG, Schenkel JM, Locquiao JJ, Fraser KA, Vezys V, Pepper M, and Masopust D (2015). Lymphocytic choriomeningitis virus persistence promotes effector-like memory differentiation and enhances mucosal T cell distribution. J. Leukoc. Biol 97, 217–225. [PubMed: 25395301]

Blackburn SD, Shin H, Freeman GJ, and Wherry EJ (2008). Selective expansion of a subset of exhausted CD8 T cells by alphaPD-L1 blockade. Proc. Natl. Acad. Sci. USA 105, 15016–15021. [PubMed: 18809920]

Bray NL, Pimentel H, Melsted P, and Pachter L (2016). Near-optimal probabilistic RNA-seq quantification. Nat. Biotechnol 34, 525–527. [PubMed: 27043002]

Buenrostro JD, Giresi PG, Zaba LC, Chang HY, and Greenleaf WJ (2013). Transposition of native chromatin for fast and sensitive epigenomic profiling of open chromatin, DNA-binding proteins and nucleosome position. Nat. Methods 10, 1213–1218. [PubMed: 24097267]

Butler A, Hoffman P, Smibert P, Papalexi E, and Satija R (2018). Integrating single-cell transcriptomic data across different conditions, technologies, and species. Nat. Biotechnol 36, 411–420. [PubMed: 29608179]

Chen Z, Ji Z, Ngiow SF, Manne S, Cai Z, Huang AC, Johnson J, Staupe RP, Bengsch B, Xu C, et al. (2019). TCF-1-Centered Transcriptional Network Drives an Effector versus Exhausted CD8 T Cell-Fate Decision. Immunity 51, 840–855.e5, e845. [PubMed: 31606264]

Daud AI, Loo K, Pauli ML, Sanchez-Rodriguez R, Sandoval PM, Taravati K, Tsai K, Nosrati A, Nardo L, Alvarado MD, et al. (2016). Tumor immune profiling predicts response to anti-PD-1 therapy in human melanoma. J. Clin. Invest 126, 3447–3452. [PubMed: 27525433]

Gehart H, and Clevers H (2019). Tales from the crypt: new insights into intestinal stem cells. Nat. Rev. Gastroenterol. Hepatol 16, 19–34. [PubMed: 30429586]

Gordon SM, Chaix J, Rupp LJ, Wu J, Madera S, Sun JC, Lindsten T, and Reiner SL (2012). The transcription factors T-bet and Eomes control key checkpoints of natural killer cell maturation. Immunity 36, 55–67. [PubMed: 22261438]

Grompe M (2012). Tissue stem cells: new tools and functional diversity. Cell Stem Cell 70, 685–689.

He R, Hou S, Liu C, Zhang A, Bai Q, Han M, Yang Y, Wei G, Shen T, Yang X, et al. (2016). Follicular CXCR5− expressing CD8(+) T cells curtail chronic viral infection. Nature 537, 412–428. [PubMed: 27501245]

Heinz S, Benner C, Spann N, Bertolino E, Lin YC, Laslo P, Cheng JX, Murre C, Singh H, and Glass CK (2010). Simple combinations of lineage-determining transcription factors prime cis-regulatory elements required for macrophage and B cell identities. Mol. Cell 38, 576–589. [PubMed: 20513432]

Huang AC, Postow MA, Orlowski RJ, Mick R, Bengsch B, Manne S, Xu W, Harmon S, Giles JR, Wenz B, et al. (2017). T-cell invigoration to tumour burden ratio associated with anti-PD-1 response. Nature 545, 60–65. [PubMed: 28397821]

Huang AC, Orlowski RJ, Xu X, Mick R, George SM, Yan PK, Manne S, Kraya AA, Wubbenhorst B, Dorfman L, et al. (2019). A single dose of neoadjuvant PD-1 blockade predicts clinical outcomes in resectable melanoma. Nat. Med 25, 454–461. [PubMed: 30804515]

Hudson WH, Gensheimer J, Hashimoto M, Wieland A, Valanparambil RM, Li P, Lin JX, Konieczny BT, Im SJ, Freeman GJ, et al. (2019). Proliferating Transitory T Cells with an Effector-like Transcriptional Signature Emerge from PD-1^{+} Stem-like $CD8^{+}$ T Cells during Chronic Infection. Immunity 51, 1043–1058.e4. [PubMed: 31810882]

Im SJ, Hashimoto M, Gerner MY, Lee J, Kissick HT, Burger MC, Shan Q, Hale JS, Lee J, Nasti TH, et al. (2016). Defining CD8+ T cells that provide the proliferative burst after PD-1 therapy. Nature 537, 417–421. [PubMed: 27501248]

Intlekofer AM, Takemoto N, Wherry EJ, Longworth SA, Northrup JT, Palanivel VR, Mullen AC, Gasink CR, Kaech SM, Miller JD, et al. (2005). Effector and memory CD8+ T cell fate coupled by T-bet and eomesodermin. Nat. Immunol 6, 1236–1244. [PubMed: 16273099]

Intlekofer AM, Banerjee A, Takemoto N, Gordon SM, Dejong CS, Shin H, Hunter CA, Wherry EJ, Lindsten T, and Reiner SL (2008). Anomalous type 17 response to viral infection by CD8+ T cells lacking T-bet and eomesodermin. Science 327, 408–411.

Jansen CS, Prokhnevska N, Master VA, Sanda MG, Carlisle JW, Bilen MA, Cardenas M, Wilkinson S, Lake R, Sowalsky AG, et al. (2019). An intra-tumoral niche maintains and differentiates stem-like CD8 T cells. Nature 576, 465–470. [PubMed: 31827286]

Joshi NS, Cui W, Chandele A, Lee HK, Urso DR, Hagman J, Gapin L, and Kaech SM (2007). Inflammation directs memory precursor and short-lived effector CD8(+) T cell fates via the graded expression of T-bet transcription factor. Immunity 27, 281–295. [PubMed: 17723218]

Kamphorst AO, Wieland A, Nasti T, Yang S, Zhang R, Barber DL, Konieczny BT, Daugherty CZ, Koenig L, Yu K, et al. (2017). Rescue of exhausted CD8 T cells by PD-1-targeted therapies is CD28-dependent. Science 355, 1423–1427. [PubMed: 28280249]

Kao C, Oestreich KJ, Paley MA, Crawford A, Angelosanto JM, Ali MA, Intlekofer AM, Boss JM, Reiner SL, Weinmann AS, and Wherry EJ (2011). Transcription factor T-bet represses expression of the inhibitory receptor PD-1 and sustains virus-specific CD8+ T cell responses during chronic infection. Nat. Immunol 12, 663–671. [PubMed: 21623380]

Khan O, Giles JR, McDonald S, Manne S, Ngiow SF, Patel KP, Werner MT, Huang AC, Alexander KA, Wu JE, et al. (2019). TOX transcriptionally and epigenetically programs $CD8^{+}$ T cell exhaustion. Nature 571, 211–218. [PubMed: 31207603]

Kurachi M, Kurachi J, Chen Z, Johnson J, Khan O, Bengsch B, Stelekati E, Attanasio J, McLane LM, Tomura M, et al. (2017). Optimized retroviral transduction of mouse T cells for in vivo assessment of gene function. Nat. Protoc 12, 1980–1998. [PubMed: 28858287]

Kurtulus S, Madi A, Escobar G, Klapholz M, Nyman J, Christian E, Pawlak M, Dionne D, Xia J, Rozenblatt-Rosen O, et al. (2019). Checkpoint Blockade Immunotherapy Induces Dynamic Changes in PD-1^{-}CD8^{+} Tumor-Infiltrating T Cells. Immunity 50, 181–194.e6, e186. [PubMed: 30635236]

Langmead B, and Salzberg SL (2012). Fast gapped-read alignment with Bowtie 2. Nat. Methods 9, 357–359. [PubMed: 22388286]

Leek JT (2014). svaseq: removing batch effects and other unwanted noise from sequencing data. Nucleic Acids Res. 42, 42.

Li H, Handsaker B, Wysoker A, Fennell T, Ruan J, Homer N, Marth G, Abecasis G, and Durbin R; 1000 Genome Project Data Processing Subgroup (2009). The Sequence Alignment/Map format and SAMtools. Bioinformatics 25, 2078–2079. [PubMed: 19505943]

Li H, van der Leun AM, Yofe I, Lubling Y, Gelbard-Solodkin D, van Akkooi ACJ, van den Braber M, Rozeman EA, Haanen JBAG, Blank CU, et al. (2019). Dysfunctional CD8 T Cells Form a Proliferative, Dynamically Regulated Compartment within Human Melanoma. Cell 176, 775–789.e18, e718. [PubMed: 30595452]

Love MI, Huber W, and Anders S (2014). Moderated estimation of fold change and dispersion for RNA-seq data with DESeq2. Genome Biol. 15, 550. [PubMed: 25516281]

McCracken MN, George BM, Kao KS, Marjon KD, Raveh T, and Weissman IL (2016). Normal and Neoplastic Stem Cells. Cold Spring Harb. Symp. Quant. Biol 81, 1–9. [PubMed: 28416577]

McKinney EF, Lee JC, Jayne DR, Lyons PA, and Smith KG (2015). T-cell exhaustion, co-stimulation and clinical outcome in autoimmunity and infection. Nature 523, 612–616. [PubMed: 26123020]

McLane LM, Abdel-Hakeem MS, and Wherry EJ (2019). CD8 T Cell Exhaustion During Chronic Viral Infection and Cancer. Annu. Rev. Immunol 37, 457–495. [PubMed: 30676822]

McLean CY, Bristor D, Hiller M, Clarke SL, Schaar BT, Lowe CB, Wenger AM, and Bejerano G (2010). GREAT improves functional interpretation of cis-regulatory regions. Nat. Biotechnol 28, 495–501. [PubMed: 20436461]

Miller BC, Sen DR, Al Abosy R, Bi K, Virkud YV, LaFleur MW, Yates KB, Lako A, Felt K, Naik GS, et al. (2019). Subsets of exhausted CD8^{+} T cells differentially mediate tumor control and respond to checkpoint blockade. Nat. Immunol 20, 326–336. [PubMed: 30778252]

Milner JJ, Toma C, Yu B, Zhang K, Omilusik K, Phan AT, Wang D, Getzler AJ, Nguyen T, Crotty S, et al. (2017). Runx3 programs CD8^{+} T cell residency in non-lymphoid tissues and tumours. Nature 552, 253–257. [PubMed: 29211713]

Muroyama Y, Nirschl TR, Kochel CM, Lopez-Bujanda Z, Theodros D, Mao W, Carrera-Haro MA, Ghasemzadeh A, Marciscano AE, Velarde E, et al. (2017). Stereotactic Radiotherapy Increases Functionally Suppressive Regulatory T Cells in the Tumor Microenvironment. Cancer Immunol. Res 5, 992–1004. [PubMed: 28970196]

Ngiow SF, Young A, Blake SJ, Hill GR, Yagita H, Teng MW, Korman AJ, and Smyth MJ (2016). Agonistic CD40 mAb-Driven IL12 Reverses Resistance to Anti-PD1 in a T-cell-Rich Tumor. Cancer Res. 76, 6266–6277. [PubMed: 27634762]

Odorizzi PM, Pauken KE, Paley MA, Sharpe A, and Wherry EJ (2015). Genetic absence of PD-1 promotes accumulation of terminally differentiated exhausted CD8+ T cells. J. Exp. Med 212, 1125–1137. [PubMed: 26034050]

Paley MA, Kroy DC, Odorizzi PM, Johnnidis JB, Dolfi DV, Barnett BE, Bikoff EK, Robertson EJ, Lauer GM, Reiner SL, and Wherry EJ (2012). Progenitor and terminal subsets of CD8+ T cells cooperate to contain chronic viral infection. Science 338, 1220–1225. [PubMed: 23197535]

Pauken KE, Sammons MA, Odorizzi PM, Manne S, Godec J, Khan O, Drake AM, Chen Z, Sen DR, Kurachi M, et al. (2016). Epigenetic stability of exhausted T cells limits durability of reinvigoration by PD-1 blockade. Science 354, 1160–1165. [PubMed: 27789795]

Pearce EL, Mullen AC, Martins GA, Krawczyk CM, Hutchins AS, Zediak VP, Banica M, DiCioccio CB, Gross DA, Mao CA, et al. (2003). Control of effector CD8+ T cell function by the transcription factor Eomesodermin. Science 302, 1041–1043. [PubMed: 14605368]

Pedregosa F, Varoquaux G, Gramfort A, Michel V, Thirion B, Grisel O, Blondel M, Prettenhofer P, Weiss R, Dubourg V, et al. (2011). Scikit-learn: Machine Learning in Python. J. Mach. Learn. Res 12, 2825–2830.

Philip M, Fairchild L, Sun L, Horste EL, Camara S, Shakiba M, Scott AC, Viale A, Lauer P, Merghoub T, et al. (2017). Chromatin states define tumour-specific T cell dysfunction and reprogramming. Nature 545, 452–456. [PubMed: 28514453]

Qiu X, Mao Q, Tang Y, Wang L, Chawla R, Pliner HA, and Trapnell C (2017). Reversed graph embedding resolves complex single-cell trajectories. Nat. Methods 14, 979–982. [PubMed: 28825705]

Roederer M, Nozzi JL, and Nason MC (2011). SPICE: exploration and analysis of post-cytometric complex multivariate datasets. Cytometry A 79, 167–174. [PubMed: 21265010]

Sade-Feldman M, Yizhak K, Bjorgaard SL, Ray JP, de Boer CG, Jenkins RW, Lieb DJ, Chen JH, Frederick DT, Barzily-Rokni M, et al. (2019). Defining T Cell States Associated with Response to Checkpoint Immunotherapy in Melanoma. Cell 176, 404. [PubMed: 30633907]

Scott AC, Dündar F, Zumbo P, Chandran SS, Klebanoff CA, Shakiba M, Trivedi P, Menocal L, Appleby H, Camara S, et al. (2019). TOX is a critical regulator of tumour-specific T cell differentiation. Nature 571, 270–274. [PubMed: 31207604]

Scott-Browne JP, López-Moyado IF, Trifari S, Wong V, Chavez L, Rao A, and Pereira RM (2016). Dynamic Changes in Chromatin Accessibility Occur in $CD8^+$ T Cells Responding to Viral Infection. Immunity 45, 1327–1340. [PubMed: 27939672]

Sen DR, Kaminski J, Barnitz RA, Kurachi M, Gerdemann U, Yates KB, Tsao HW, Godec J, LaFleur MW, Brown FD, et al. (2016). The epigenetic landscape of T cell exhaustion. Science 354, 1165–1169. [PubMed: 27789799]

Seo H, Chen J, González-Avalos E, Samaniego-Castruita D, Das A, Wang YH, López-Moyado IF, Georges RO, Zhang W, Onodera A, et al. (2019). TOX and TOX2 transcription factors cooperate with NR4A transcription factors to impose $CD8^+$ T cell exhaustion. Proc. Natl. Acad. Sci. USA 116, 12410–12415. [PubMed: 31152140]

Siddiqui I, Schaeuble K, Chennupati V, Fuertes Marraco SA, Calderon-Copete S, Pais Ferreira D, Carmona SJ, Scarpellino L, Gfeller D, Pradervand S, et al. (2019). Intratumoral $Tcf1^+PD\text{-}1^+CD8^+$ T Cells with Stem-like Properties Promote Tumor Control in Response to Vaccination and Checkpoint Blockade Immunotherapy. Immunity 50, 195–211.e10, e110. [PubMed: 30635237]

Taqueti VR, Grabie N, Colvin R, Pang H, Jarolim P, Luster AD, Glimcher LH, and Lichtman AH (2006). T-bet controls pathogenicity of CTLs in the heart by separable effects on migration and effector activity. J. Immunol 177, 5890–5901. [PubMed: 17056513]

Thommen DS, Koelzer VH, Herzig P, Roller A, Trefny M, Dimeloe S, Kiialainen A, Hanhart J, Schill C, Hess C, et al. (2018). A transcriptionally and functionally distinct $PD\text{-}1^+$ $CD8^+$ T cell pool with predictive potential in non-small-cell lung cancer treated with PD-1 blockade. Nat. Med 24, 994–1004. [PubMed: 29892065]

Utzschneider DT, Charmoy M, Chennupati V, Pousse L, Ferreira DP, Calderon-Copete S, Danilo M, Alfei F, Hofmann M, Wieland D, et al. (2016). T Cell Factor 1-Expressing Memory-like CD8(+) T Cells Sustain the Immune Response to Chronic Viral Infections. Immunity 45, 415–427. [PubMed: 27533016]

Wu T, Ji Y, Moseman EA, Xu HC, Manglani M, Kirby M, Anderson SM, Handon R, Kenyon E, Elkahloun A, et al. (2016). The TCF1-Bcl6 axis counteracts type I interferon to repress exhaustion and maintain T cell stemness. Sci. Immunol 1, 1.

Wu TD, Madireddi S, de Almeida PE, Banchereau R, Chen YJ, Chitre AS, Chiang EY, Iftikhar H, O'Gorman WE, Au-Yeung A, et al. (2020). Peripheral T cell expansion predicts tumour infiltration and clinical response. Nature 579, 274–278. [PubMed: 32103181]

Wykes MN, and Lewin SR (2018). Immune checkpoint blockade in infectious diseases. Nat. Rev. Immunol 18, 91–104. [PubMed: 28990586]

Yao C, Sun HW, Lacey NE, Ji Y, Moseman EA, Shih HY, Heuston EF, Kirby M, Anderson S, Cheng J, et al. (2019). Single-cell RNA-seq reveals TOX as a key regulator of $CD8^+$ T cell persistence in chronic infection. Nat. Immunol 20, 890–901. [PubMed: 31209400]

Yost KE, Satpathy AT, Wells DK, Qi Y, Wang C, Kageyama R, McNamara KL, Granja JM, Sarin KY, Brown RA, et al. (2019). Clonal replacement of tumor-specific T cells following PD-1 blockade. Nat. Med 25, 1251–1259. [PubMed: 31359002]

Zander R, Schauder D, Xin G, Nguyen C, Wu X, Zajac A, and Cui W (2019). $CD4^+$ T Cell Help Is Required for the Formation of a Cytolytic $CD8^+$ T Cell Subset that Protects against Chronic Infection and Cancer. Immunity 51, 1028–1042.e4. [PubMed: 31810883]

Zhang L, Yu X, Zheng L, Zhang Y, Li Y, Fang Q, Gao R, Kang B, Zhang Q, Huang JY, et al. (2018). Lineage tracking reveals dynamic relationships of T cells in colorectal cancer. Nature 564, 268–272. [PubMed: 30479382]

Highlights

- Ly108 and CD69 define four Tex subsets linked in a hierarchical developmental pathway
- Two TCF1+ subsets, effector-like and terminally exhausted subsets, are identified
- Key transcriptional, epigenetic, and biological changes define subset transitions
- TCF1, T-bet, and Tox coordinate Tex subset development and dynamics

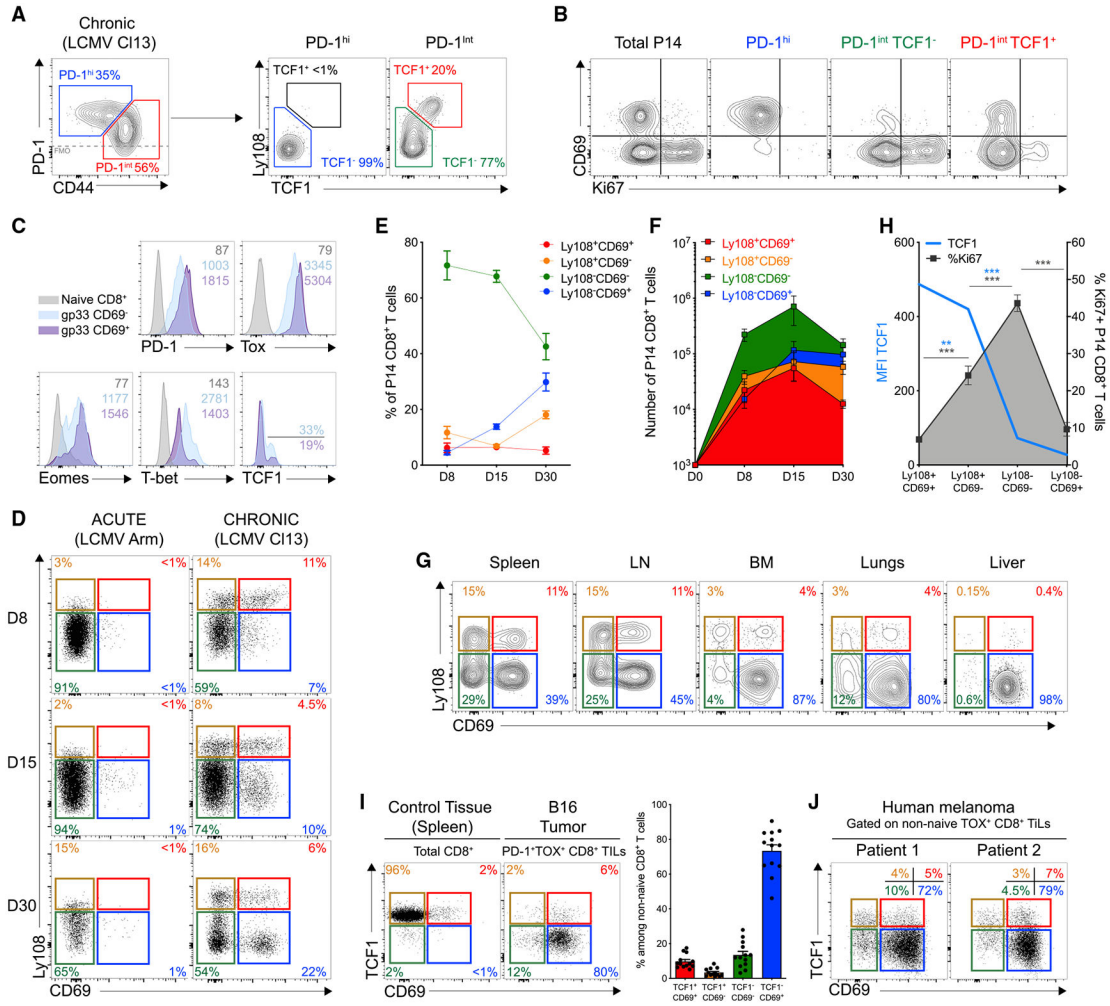

Figure 1. Four Tex Subsets Develop during Chronic Viral Infections and Cancer

Naive CD45.1$^+$ P14 CD8$^+$ T (10^3) were adoptively transferred into C57BL/6J mice (CD45.2$^+$) after infection with LCMV clone 13 and analyzed at d30pi.

(A) Ly108 and TCF1 expression by PD-1^{int} and PD-1^{hi} P14 CD8$^+$ T cells. Numbers are frequencies.

(B) Representative Ki67 and CD69 co-expression in indicated populations of P14 CD8$^+$ T cells.

(C) Representative histograms for indicated markers on subpopulations among endogenous D^{b}gp33 tetramer$^+$ CD8$^+$ T cells. Numbers are mean fluorescence intensity (MFI).

(D) Representative Ly108 and CD69 co-expression on splenic P14 CD8$^+$ T cells at indicated time post-infection (pi) with LCMV Armstrong (left) or clone 13 (right). Numbers are frequencies.

(E) Frequencies of different P14 populations at indicated time after clone-13 infection.

(F) Absolute number of different P14 populations at indicated time after clone-13 infection.

(G) Representative Ly108 and CD69 co-expression in tissues. Numbers are frequencies.

(H) Frequencies of Ki67$^+$ cells among indicated P14 populations (gray line; right axis) and MFI for TCF1 (blue line; left axis).

(I) Representative TCF1 and CD69 co-expression on PD-1^{+}Tox^{+} TILs from B16 tumors (see Figure S1I for gating). Right graph shows cumulative data.
(J) Representative TCF1 and CD69 co-expression on non-naive Tox^{+} TILs (see Figure S1J for gating) analyzed from human melanoma tumors. n = 7 patients.
(A)–(H), n = 5 with 6 to 16 mice per group/time point.
(I), n = 2 with 11 mice/group.

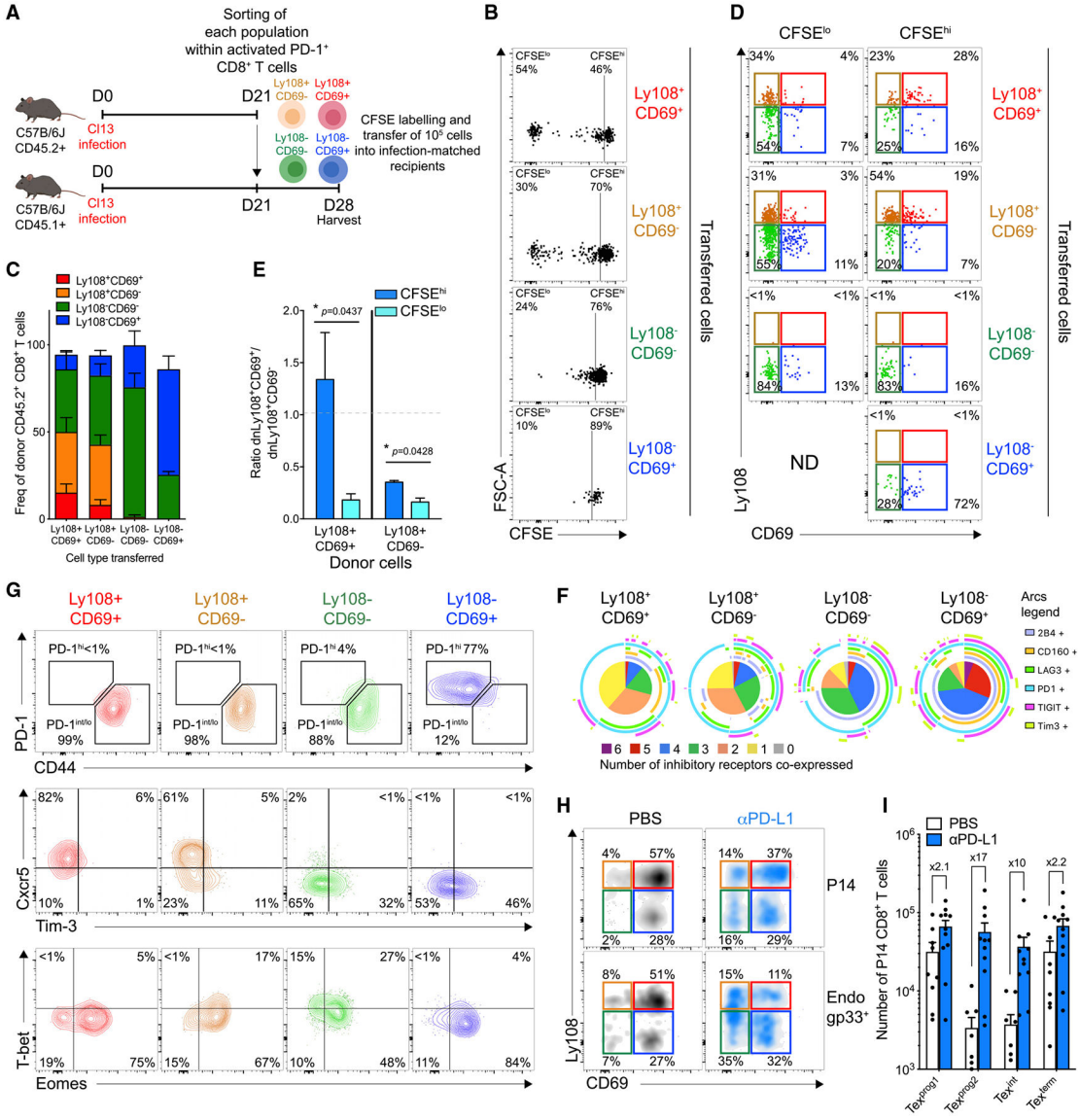

Figure 2. Developmental Lineage Relationships between Four Tex Subsets and Changes upon PD-L1 Blockade

(A) Experimental design. Tex subsets were sorted from endogenous PD-1$^+$ CD8$^+$ T cells at d21pi, labeled with CFSE, transferred back (1×10^5 each) into infection-matched recipients and analyzed 7 days post-transfer (d28pi).

(B) CFSE profile of indicated transferred populations. Numbers are frequencies.

(C) Frequencies of P14 populations from indicated donor cells.

(D) Ly108 and CD69 co-expression on divided (CFSE^{lo}) and undivided (CFSE^{hi}) cells that developed from indicated transferred cells.

(E) Ratio of Ly108$^+$CD69$^+$/Ly108$^+$CD69$^-$ within CFSE^{lo} (light blue) and CFSE^{hi} (dark blue) cells from indicated donor origin.

(F) IRs co-expression on indicated P14 populations.

(G) Representative PD-1/CD44, Cxcr5/Tim-3, and T-bet/Eomes co-expression in indicated P14 populations.

(H) Representative Ly108 and CD69 co-expression on P14 ($CD45.1^+$) and endogenous D^bgp33^+ ($CD45.2^+$) $CD8^+$ T cells 1 day after treatment (d35pi) with either PBS (CTR) or anti-PD-L1.

(I) Absolute number of indicated P14 populations 1 day post-treatment (d35pi) with either PBS (CTR) or anti-PD-L1.

(B)–(E), n = 2 with 6–8 mice/group; (F), n = 3 with 10 mice/group; (G), n = 2 with 9 mice/group; (H) and (I), n = 2 with 7–11 mice/group.

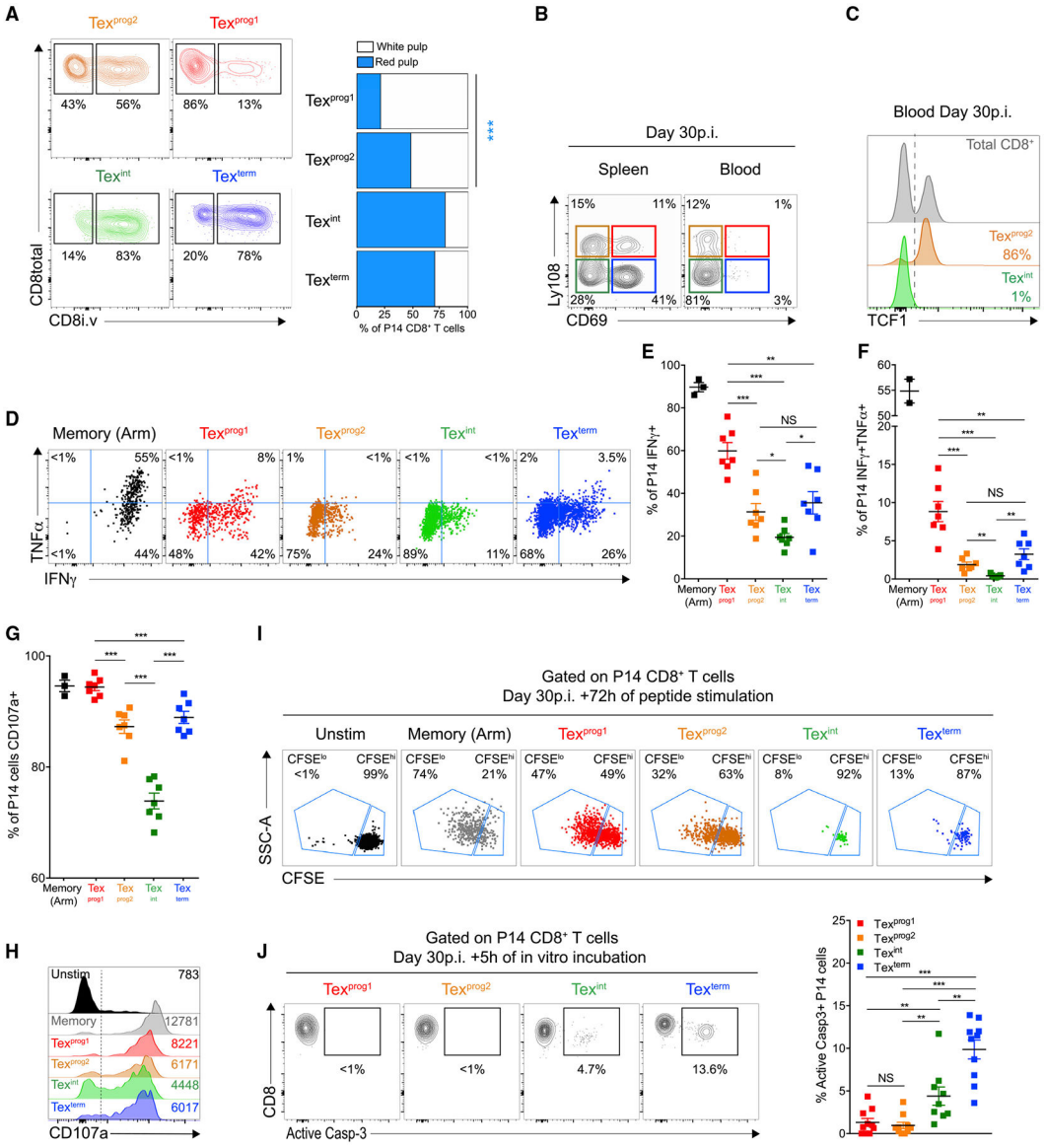

Figure 3. Developmental Transitions Alter Tex Subset Localization and Effector Functions

(A) LCMV-clone-13-infected mice were injected with 3μg/mouse of anti-CD8 i.v. at d30pi and sacrificed 3 min later. Representative dot plots (left) and frequencies (right) of indicated P14 populations located either in the white pulp (CD8 i.v. antibody negative) or the red pulp (CD8 i.v. antibody positive) of the spleen. Numbers are frequencies.

(B) Representative Ly108 and CD69 co-expression on P14 $CD8^+$ T cells isolated from the spleen (left plot) or blood (right plot). Numbers are frequencies.

(C) TCF1 expression in indicated P14 populations isolated from the blood.

(D) Representative IFNγ and TNF co-production by indicated P14 populations at d30pi. Numbers are frequencies.

(E–G) Frequencies of IFNγ+ (E), IFNγ+TNFα+ (F), and CD107a+ (G) cells among indicated P14 populations.

(H) Representative CD107a expression by indicated P14 populations. Numbers are MFI.

(I) Indicated P14 populations were sorted at d30pi, labeled with CFSE, and incubated with gp33-peptide coated dendritic cells (ratio 1/1). Dot plots display CFSE dilution profile after 3 days of co-culture. Numbers are frequencies.

(J) Representative dot plots and frequencies of active caspase-3-positive cells within indicated P14 populations. Numbers are frequencies.

(A)–(C), 3 independent experiments with 12–18 mice/group; (D)–(H), n = 2 with 7 mice/group; (I), n = 2 with 4–10 mice/group; (J), n = 3 with 10 mice/group.

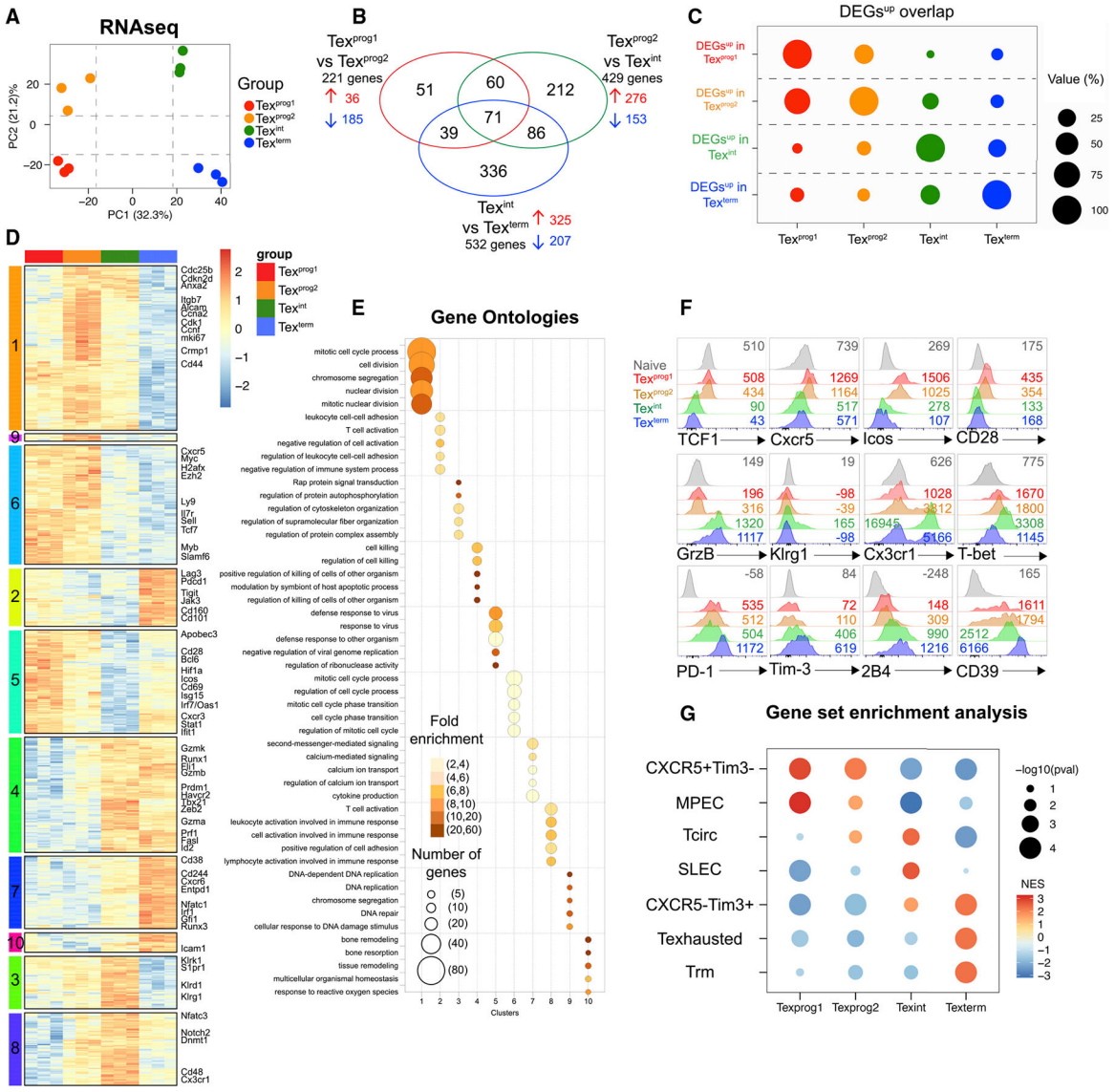

Figure 4. Subset Transitions Induce Major Transcriptional Changes and Drive Acquisition of Population-Specific Transcriptomic Signatures

(A) PCA of RNA-seq profiles.

(B) Venn diagram displaying overlaps between DEGs from indicated pairwise comparisons (lfc ≥ 1, p = 0.01).

(C) DEGs^{UP} overlaps between indicated P14 populations. Bubble size represents the proportion of DEGs^{UP} from each individual Tex population (y axis) also found to be upregulated in indicated Tex subsets (x axis) in at least one pairwise comparison.

(D) Heatmap displaying all DEGs (lfc ≥ 1, p = 0.01) clustered by using Pearson correlation as distance measure. Color legend indicates row z scores.

(E) Pathway enrichment analysis. Bubble graph displays the five most significantly enriched pathways by log(q-value) for each cluster established in Figure 4D.

(F) Representative histograms showing the expression of indicated markers by different P14 populations. Numbers are MFIs.

(G) GSEA displaying enrichment of each individual Tex subset for signatures of indicated cell types. NES, Normalized Enrichment Score.
n = 3 biological replicates.

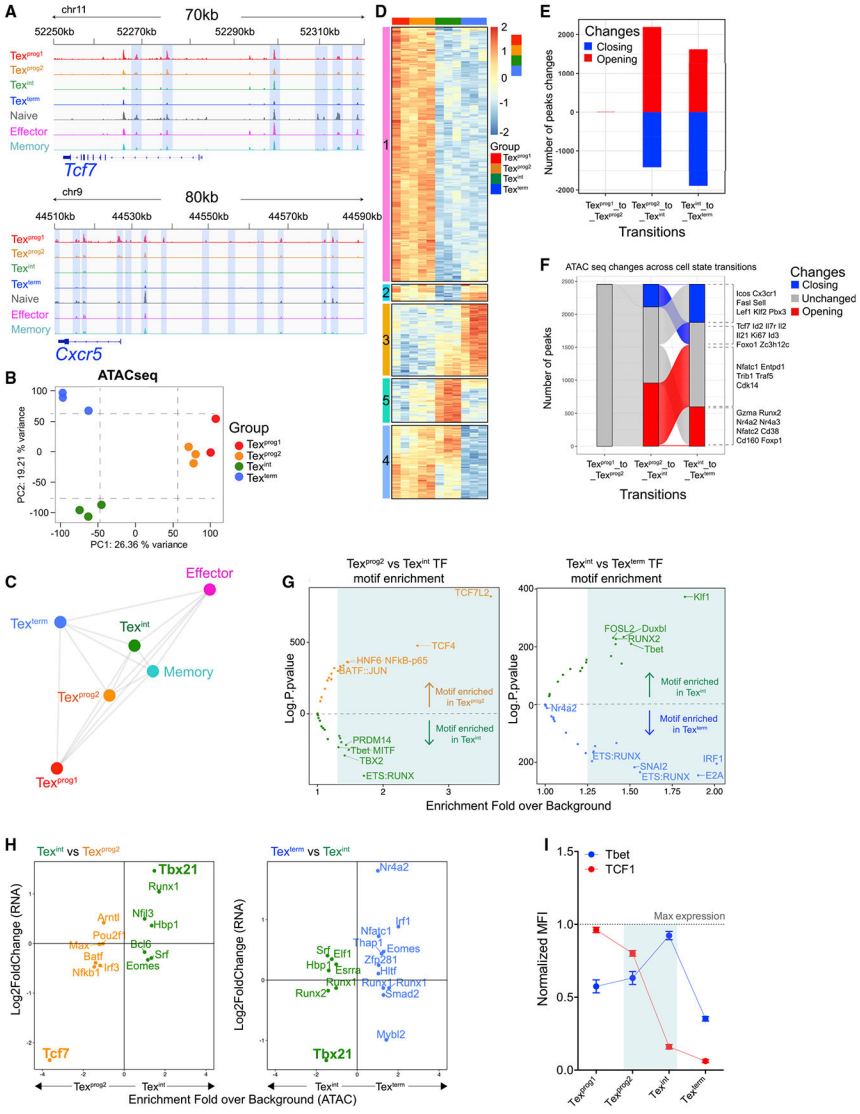

Figure 5. Epigenetic Remodeling during Tex Subset Transitions Identifies Subset-Specific TF Accessibility

(A) ATAC-seq tracks at indicated loci.

(B) PCA of normalized ATAC-seq counts (top 25% peaks by variance are displayed).

(C) Spearman correlation network analysis showing similarities between indicated populations based on all ATAC-seq peaks.

(D) Heatmap of peak intensity displaying the top 500 peaks by variance and clustered by using *K*-means method (k = 5). Color legend indicates row *z* scores.

(E) Number of statistically significant peaks (lfc ≥ 1, p < 0.05) either opening (red) or closing (blue) upon indicated subset transitions.

(F) Alluvial plot displaying the dynamics of transition-specific peaks (E) and refined as lfc ≥ 1, p < 0.01.

(G) TF motifs enrichment analysis (HOMER) of subset-transition specific peaks (E). Volcano plots show TFs with the highest predicted binding activity to the identified DNA sequence.

(H) Comparing TF motif enrichment with differential mRNA expression (Log2FoldChange) upon the indicated subset-transition. Plotted are TFs with a motif enrichment fold over background >1.25 in (G).

(I) Protein expression dynamics of TCF1 and T-bet in the indicated P14 populations at d30pi.

(A)–(H), n = 3 biological replicates; (I), n = 2 with 7mice/group.

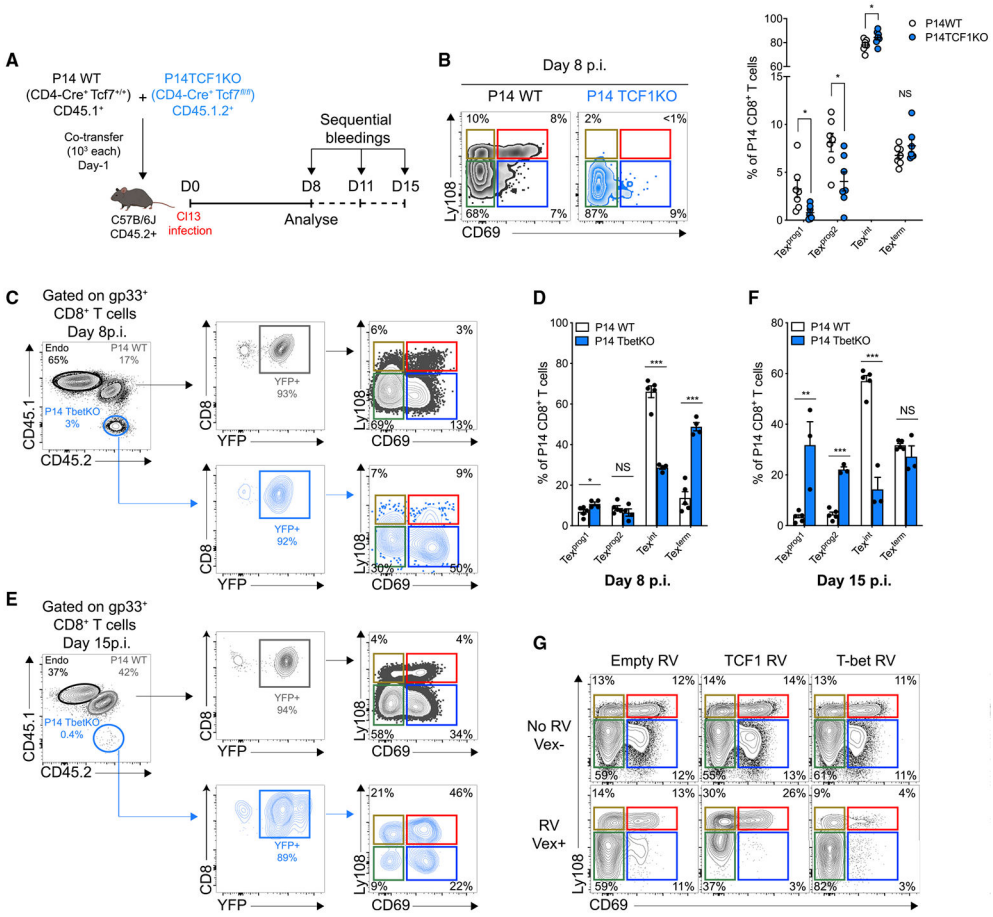

Figure 6. TCF1 and T-bet Mediate Opposing Regulation of Tex Subset Differentiation

(A) Experimental design.

(B) Representative flow cytometry plots (left) and frequencies (right) of indicated populations among splenic WT (gray; open circles) or TCF1KO (blue) P14 CD8$^+$ T cells at d8pi. Numbers are frequencies.

(C–F) Gating strategy, representative flow cytometry plots and frequencies of indicated populations of WT P14 (gray; open bars) or T-bet KO P14 (blue) at d8 ([C] and [D]) and 15 ([E] and [F]) pi. Numbers are frequencies.

(G) Representative Ly108 and CD69 co-expression by P14 CD8$^+$ T cells transduced (VEX+; lower line) or not (VEX−; upper line) with either empty (Empty RV), TCF1 (short isoform; TCF1 RV), or T-bet (Tbet RV) encoding RVs at d15pi. Numbers are frequencies.

(B), n = 2 with 7 mice/group; (C)–(F), n = 3–5 with 11–17 mice/group; (G), n = 1 with 4 mice/group.

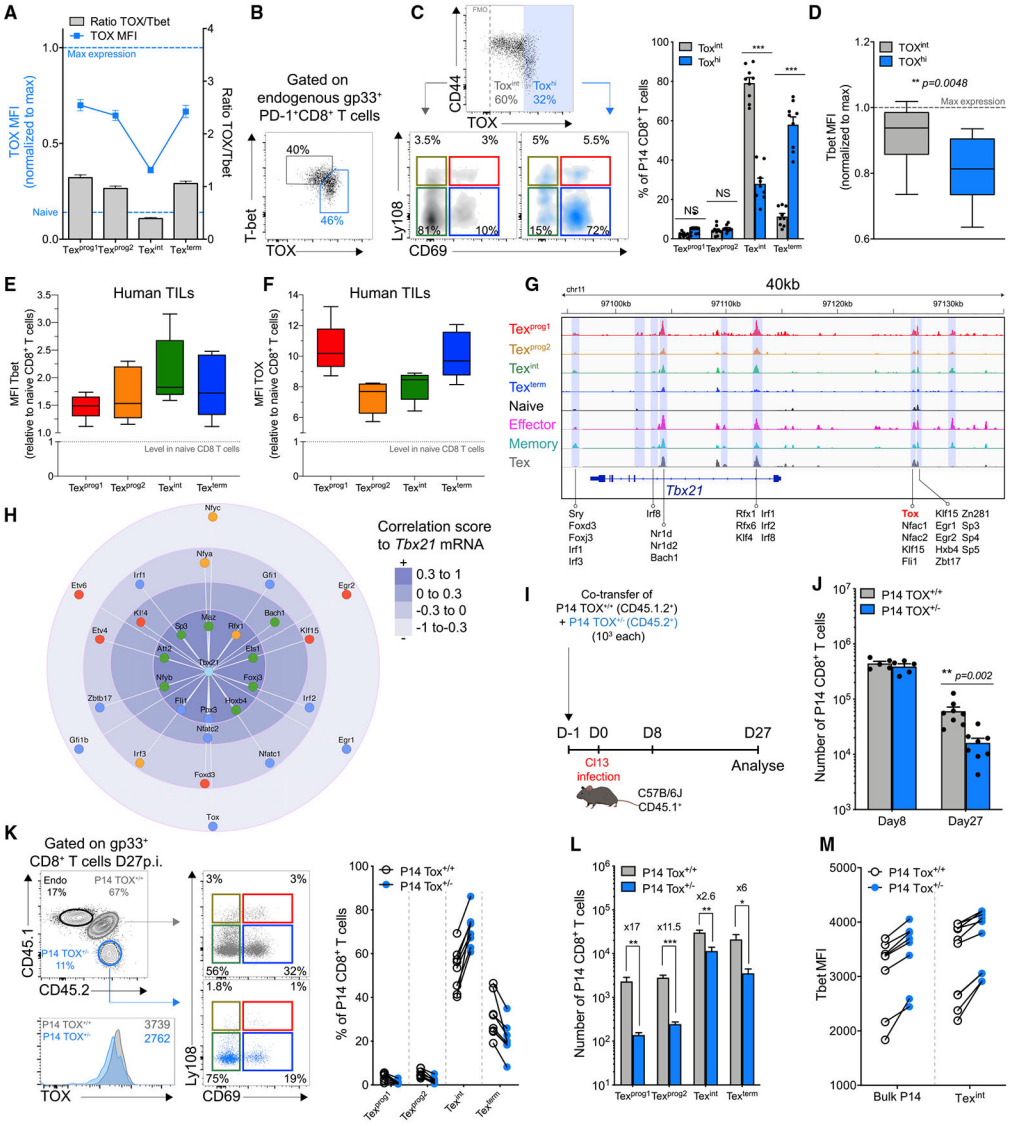

Figure 7. Tox Modulates Tex Subset Dynamics through Regulation of T-bet

(A) Tox MFI (blue line; left axis) and Tox/T-bet ratio (gray bars; right axis) in indicated populations among D^bgp33 tetramer$^+$CD8$^+$ T cells at d27pi.

(B) Representative T-bet and Tox co-expression in PD-1$^+$ D^bgp33 tetramer$^+$ CD8$^+$ T cells at d27pi.

(C) Representative plots (left) and frequency (right) of indicated populations among Tox^{int} (gray) and Tox^{hi} (blue) endogenous D^bgp33 tetramer$^+$ CD8$^+$ T cells.

(D) T-bet MFI in Tox^{int} and Tox^{hi} endogenous D^bgp33 tetramer$^+$ CD8$^+$ T cells.

(E and F) T-bet (E) and Tox (F) MFI in indicated populations (gated on TCF1 and CD69; Figure 1J) within non-naive Tox$^+$ TILs isolated from human melanoma tumors.

(G) ATACseq tracks at the *Tbx21* locus highlighting TFs with predictive binding sites at the indicated OCRs.

(H) Correlation score by mRNA between T-bet and TFs predicted to bind near the *Tbx21* locus (filtering out TFs without detectable mRNA in Tex subsets). Each TF is colored by the

cell-type in which mRNA expression is highest (red-Tex^{prog1}, orange Tex^{prog2}, green-Tex^{int}, blue-Tex^{term}).

(I) Experimental design.

(J) Numbers of $Tox^{+/+}$ P14 (gray) and $Tox^{+/-}$ P14 (blue) cells at the indicated time points.

(K) Representative dot plots (left) and frequencies (right) of the indicated populations among $Tox^{+/+}$ (gray; open circles) and $Tox^{+/-}$ (blue) P14 cells. Numbers indicate frequencies. Numbers in the histogram are MFI.

(L) Number of indicated populations within $Tox^{+/+}$ P14 (gray) and $Tox^{+/-}$ P14 (blue) at d27pi.

(M) T-bet MFI in indicated populations among $Tox^{+/+}$ P14 (open circles) and $Tox^{+/-}$ P14 (blue circles). Linked circles represent individual mice.

(A)–(D), 3 experiments with 22 mice/group; (E) and (F), n = 7 patients; (J)–(M), 2 experiments with 15 mice/group.

KEY RESOURCES TABLE

REAGENT or RESOURCE	SOURCE	IDENTIFIER
Antibodies (Mouse, Human, Intracellular, *In Vivo*)		
FITC mouse anti-mouse CD244 (clone 2B4)	BD Biosciences	Cat# 553305; RRID: AB_394769
FITC Hamster anti-mouse KLRG1 (clone 2F1)	SouthernBiotech	Cat# 1807-02; RRID: AB_2795367
Alexa Fluor 488 anti-mouse CD45 (clone 30-F11)	Biolegend	Cat# 103122; RRID: AB_493531
Alexa Fluor 488 anti-mouse Ly-6C (clone HK1.4)	Biolegend	Cat# 128022; RRID: AB_10639728
PE/Dazzle 594 anti-mouse TIGIT (clone 1G9)	Biolegend	Cat# 142110; RRID: AB_2566573
PE-CF594 rat anti-mouse CD127 (clone SB/199)	BD Biosciences	Cat# 562419; RRID: AB_11153131
PE-Cyanine 5 anti-mouse/rat ICOS (clone C398.4A)	Ebioscience	Cat# 15-9949-82; RRID: AB_468828
PE/Cy5 anti-mouse CD69 (clone H1.2F3)	Biolegend	Cat# 104510; RRID: AB_313113
PE-Cyanine7 anti-mouse CD28 (clone 37.51)	Ebioscience	Cat# 25-0281-82; RRID: AB_469612
PE/Cy7 anti-mouse CD279 (PD-1, clone RMP1-30)	Biolegend	Cat# 109110; RRID: AB_572017
PE anti-mouse Ly108 (clone 330-AJ)	Biolegend	Cat# 134606; RRID: AB_2188095
PE anti-mouse CD160 (clone 7H1)	Biolegend	Cat# 143004; RRID: AB_10960743
APC anti-mouse CD223 (Lag-3, clone eBioC9B7W)	Ebioscience	Cat# 17-2231-82; RRID: AB_2573184
Alexa Fluor 647 anti-mouse/human CD44 (clone IM7)	Biolegend	Cat# 103018; RRID: AB_493681
APC-eFluor 780 anti-mouse CD62L (clone MEL-14)	Ebioscience	Cat# 47-0621-82; RRID: AB_1603256
APC-eFluor 780 anti-mouse KLRG1 (clone 2F1)	Ebioscience	Cat# 47-5893-82; RRID: AB_2573988
APC-eFluor 780 anti-human/mouse CD44 (clone IM7)	Ebioscience	Cat# 47-0441-82; RRID: AB_1272244
APC-Cy7 rat anti-mouse CD25 (clone PC61)	BD Biosciences	Cat# 557658; RRID: AB_396773
APC-eFluor 780 anti-mouse CD4 (clone RM4-5)	Ebioscience	Cat# 47-0042-82; RRID: AB_1272183
Alexa Fluor 700 anti-mouse CD45.1 (clone A20)	Biolegend	Cat# 110724; RRID: AB_493733
eFluor 450 anti-mouse CD223 (Lag-3, clone eBioC9B7W)	Ebioscience	Cat# 48-2231-82; RRID: AB_11149866
eFluor 450 anti-mouse CD8a (clone 53-6.7)	Ebioscience	Cat# 48-0081-82; RRID: AB_1272198
Pacific Blue anti-mouse Ly108 (clone 330-AJ)	Biolegend	Cat# 134608; RRID: AB_2188093
Brillant Violet 605 anti-mouse CD4 (clone RM4-5)	Biolegend	Cat# 100548; RRID: AB_2563054
Brillant Violet 605 anti-mouse CX3CR1 (clone SA011F1)	Biolegend	Cat# 149027; RRID: AB_2565937
Brillant Violet 605 anti-mouse CD366 (Tim-3, clone RMT3-23)	Biolegend	Cat# 119721; RRID: AB_2616907
Brillant Violet 650 anti-mouse CD8a (clone 53-6.7)	Biolegend	Cat# 100742; RRID: AB_2563056
Brillant Violet 785 anti-mouse CD45.2 (clone 104)	Biolegend	Cat# 109839; RRID: AB_2562604
Purified anti-mouse CD16/32 Antibody	Biolegend	Cat#101302; RRID: AB_312801
Ultra-LEAF purified anti-mouse CD28 (clone 37.51)	Biolegend	Cat#102116; RRID: AB_11147170
LEAF purified anti-mouse CD3ε (clone 145-2C11)	Biolegend	Cat#100331; RRID: AB_1877073
BUV395 Mouse Anti-Human CD45RA (clone HI100)	BD Biosciences	Cat#740298; RRID: AB_2740037
BUV496 Mouse Anti-Human CD8 (clone RPA-T8)	BD Biosciences	Cat#564805; RRID: AB_2744460
BUV737 Mouse Anti-Human CD27 (clone L128)	BD Biosciences	Cat#564302; RRID: AB_2744350
BUV805 Mouse Anti-Human CD3 (clone UCHT1)	BD Biosciences	Cat#565515; RRID: AB_2739277
PE/Cy5 anti-human CD69 Antibody (clone FN50)	Biolegend	Cat#310908; RRID: AB_314843
PE Anti-TOX antibodies, human and mouse (clone REA473)	Miltenyi	Cat#130-107-785; RRID: AB_2654225
Alexa Fluor® 647 anti-TCF1 (TCF7) Antibody (clone C63D9)	Cell Signaling Technology	Cat#6709S; RRID: AB_2797631
Brilliant Violet 605™ anti-T-bet Antibody (clone 4B10)	Biolegend	Cat#644817; RRID: AB_11219388

REAGENT or RESOURCE	SOURCE	IDENTIFIER
Alexa Fluor 700 Mouse anti-Ki-67 (clone B56)	BD Biosciences	Cat# 561277; RRID: AB_10611571
FITC Rabbit Anti-Active Caspase-3 (clone C92-605)	BD Biosciences	Cat# 560901; RRID: AB_10563896
PE/Cy7 anti-human CD279 (PD-1) Antibody (clone EH12.2H7)	Biolegend	Cat#329918; RRID: AB_2159324
Eomes Monoclonal Antibody, PEeFluor 610, eBioscience™ (clone WD1928)	Ebioscience	Cat# 61-4877-42; RRID: AB_2574616
Alexa Fluor 488 anti-mouse CD107a (LAMP-1, clone 1D4B)	Biolegend	Cat# 121608; RRID: AB_571983
FITC mouse anti-Ki67 (clone B56)	BD Biosciences	Cat# 51-36524X; RRID: AB_396302
FITC anti-T-bet (clone 4B10)	Biolegend	Cat# 644812; RRID: AB_2200540
R-PE conjugate anti-human Granzyme B (clone GB12)	Invitrogen	Cat# MHGB04; RRID: AB_1500191
PE Rabbit anti-active Caspase-3 (clone C92-605)	BD Biosciences	Cat# 51-68655X; RRID: AB_393957
PE mouse anti-TCF-7/TCF-1 (clone S33-966)	BD Biosciences	Cat# 564217; RRID: AB_2687845
PE-Cy7 anti-mouse TNFa (clone MP6-XT22)	Ebioscience	Cat# 25-7321-82; RRID: AB_11042728
APC anti-mouse IFNg (clone XMG1.2)	Ebioscience	Cat# 17-7311-82; RRID: AB_469504
APC anti-TOX human and mouse (clone REA473)	Miltenyi Biotech	Cat# 130-118-335; RRID: AB_2751485
In vivo Mab anti-mouse CD4 (clone GK1.5)	BioXcell	Cat# BE0003-1; RRID: AB_1107636
In vivo Mab anti-mouse PD-L1 (clone 10F.9G2)	BioXcell	Cat# BE0101; RRID: AB_10949073
Bacterial and Virus Strains		
LCMV clone 13	Rafi Ahmed	Grew up in house
LCMV Armstrong (Arm)	Rafi Ahmed	Grew up in house
Biological Samples		
Patients samples used in this study are detailed elsewhere (Huang et al., 2019)	N/A	N/A
Chemicals, Peptides, and Recombinant Proteins		
Live/Dead Fixable Aqua Dead cell stain Kit	ThermoFisher Scientific	Cat# L34957
Zombie NIR Fixable viability kit	Biolegend	Cat# 423105
CellTrace CFSE Cell Proliferation Kit	ThermoFisher Scientific	Cat# C34554
Recombinant Murine IL-2	Peprotech	Cat#212-12
ACK Lysing Buffer	ThermoFisher Scientific	Cat#A1049201
Collagenase, Type 4	Worthington	Cat#LS004189
Deoxyribonuclease I from bovine pancreas	Sigma-Aldrich	Cat#D5025
Collagenase D	Roche	Cat#11088866001
Golgi Stop	BD Biosciences	Cat#554724
Golgi Plug	BD Biosciences	Cat#555029
gp (33-41) peptide KAVYNFATM	GenScript	Custom
OVA (257-264) peptide SIINFEKL	GenScript	Custom
LCMV tetramers (gp33, gp276)	NIH	N/A
Percoll®	Sigma-Aldrich	Cat#GE17-0891-01
Histopaque®-1083	Sigma-Aldrich	Cat#10831
Tat-cre Recombinase	Protein and Proteomics Core Facility, The Children's Hospital of Philadelphia	N/A
NEBNext High-Fidelity 2X PCR Master Mix	New England Biolabs	Cat#M0541
Cell Culture Reagents		

REAGENT or RESOURCE	SOURCE	IDENTIFIER
RPMI-1640 medium	Corning/Mediatech	Cat#10-040-CV
HI Fetal Bovine Serum	ThermoFisher	Cat#26170-043
HEPES	ThermoFisher	Cat#15630080
Non-Essential Amino Acids	ThermoFisher	Cat#11140050
Penicillin-Streptomycin	ThermoFisher	Cat#15140122
β-mercaptoethanol	Sigma-Aldrich	Cat#M6250-500ML
Opti-MEM	ThermoFisher	Cat#31985088
Polybrene	Sigma-Aldrich	Cat#TR-1003-G
Lipofectamine 3000 transfection reagent	ThermoFisher	Cat#L3000001
Critical Commercial Assays		
Fixation/Permeabilization Solution Kit	BD Biosciences	Cat#554714
Foxp3 / Transcription Factor Staining Buffer Set	BD Biosciences	Cat#00-5523-00
RNeasy Micro Kit	QIAGEN	Cat#74004
High Sensitivity RNA ScreenTape	Agilent	Cat#5067-5579
Agencourt AMPure XP	Beckman	Cat#A63880
High sensitivity D5000 screentape	Agilent	Cat#5067-5592
Library Quantification Kit	Kapabiosystems	Cat#KK4824
EasySep Mouse $CD8^+$ T Cell Isolation Kit	StemCell Technologies	Cat#19853
MinElute Reaction Cleanup Kit	QIAGEN	Cat#28204
QIAquick PCR Purification Kit	QIAGEN	Cat#28104
Nextera DNA Library Preparation Kit	Illumina	Cat#FC-121-1030
SMART-Seq® v4 Ultra® Low Input RNA Kit for Sequencing	Takara/Clontech	Cat#634889
Nextera XT DNA Library Preparation Kit	Illumina	Cat#FC-131-1024
NSQ 500 Hi Output KT v2 (150 CYS)	Illumina	Cat#FC-404-2002
D1000 ScreenTape	Agilent	Cat#5067-5582
Deposited Data		
RNAseq and ATACseq for the Ly108- and CD69-defined Tex subsets (d30pi)	In this paper	GEO: GSE149879
RNaseq for Cxcr5+Tim3− and Cxcr5−Tim3+ CD8s	Im et al., 2016	GEO: GSE84105
RNaseq for MPEC and SLEC	Joshi et al., 2007	GEO: GSE8678
Teff and Tmem transcriptional signature	Scott-Browne et al., 2016	GEO: GSE88987
Mouse TILs transcriptional signature	Philip et al., 2017	GEO: GSE89307
ATACseq profile of Teff and Tmem	Pauken et al., 2016	GEO: GSE86797
10X single-cell RNASeq profiling of GP33-tetramer+ $CD8^+$ T cells from mice chronically infected with LCMV Clone 13	Miller et al., 2019	GEO: GSE122712
Experimental Models: Cell Lines		
B16 melanoma cell line	Grown in house	N/A
MC-38 colon adenocarcinoma cell line	Grown in house	N/A
Experimental Models: Organisms/Strains		
C57BL/6 mice	NCI/Charles River	Cat#027
B6-Ly5.1/Cr	NCI/Charles River	Cat#564
B6.SJL-*Ptprca Pepcb*/BoyJ	The Jackson Laboratory	Cat#002014

REAGENT or RESOURCE	SOURCE	IDENTIFIER
P14 Tg mice	Bred in house (NCI background)	N/A
CD4-cre	The Jackson Laboratory	Cat#022071
P14 *Tcf7*$^{flox/flox}$ CD4-Cre	In this paper	N/A
P14 *Tbx21*$^{flox/flox}$ ERT2-Cre$^{+/-}$ Rosa-YFP$^{+/-}$ mice	In this paper	N/A
P14 *Tox*$^{+/-}$	In this paper	N/A
Recombinant DNA		
TCF-1 p33 cDNA	OriGene	Cat#MR226713
TCF-1 p33 overexpression vector	In this paper	N/A
T-bet overexpression vector	In this paper	N/A
Empty-VEX retroviral vector	Kurachi et al., 2017	N/A
Software and Algorithms		
FlowJo V10.4.2	TreeStar	https://www.flowjo.com/solutions/flowjo/downloads
GraphPad Prism v6	GraphPad Software	https://www.graphpad.com/scientific-software/prism/
Biorender	Biorender Software	https://biorender.com/
Pestle v1.8	NIH/NIAID (Roederer et al., 2011)	On demand
Spice v5.35	NIH/NIAID (Roederer et al., 2011)	https://niaid.github.io/spice/help/dataformat
IGV v2.4.16	The Broad Institute	https://software.broadinstitute.org/software/igv/download
Datagraph	Visual Data Tools	https://www.visualdatatools.com/DataGraph/Download/
Cytoscape (v3.4)	Cytoscape	https://cytoscape.org/download.html
GSEA (v3.0)	The Broad Institute	http://software.broadinstitute.org/gsea/index.jsp
Monocle (v2)	Qiu et al., 2017	http://cole-trapnell-lab.github.io/monocle-release/docs/
Homer (v4.6)	Heinz et al., 2010	http://homer.ucsd.edu/homer/download.html
Bowtie (v2)	Langmead and Salzberg, 2012	http://bowtie-bio.sourceforge.net/index.html
Samtools (v1.1)	Li et al., 2009	http://samtools.sourceforge.net/
Kallisto (v0.44)	Bray et al., 2016	https://pachterlab.github.io/kallisto/download
Deseq2 1.22.2	Love et al., 2014	http://www.bioconductor.org/packages/release/bioc/html/DESeq2.html
svaseq	Leek, 2014	https://bioconductor.org/packages/release/bioc/html/sva.html
Pheatmap	Bioconductor	https://cran.r-project.org/web/packages/pheatmap/index.html
Great (v3.0)	McLean et al., 2010	http://great.stanford.edu/public/html/
ggplot2 (v3.2.0)	R package	https://cran.r-project.org/web/packages/ggplot2/index.html
Seurat_3.1.1	Butler et al., 2018	https://cran.r-project.org/web/packages/Seurat/index.html